Eur. Phys. J. C 49, 919–945 (2007)
DOI 10.1140/epjc/s10052-006-0166-6

THE EUROPEAN PHYSICAL JOURNAL C

Regular Article – Experimental Physics

Charged pion production in p+C collisions at 158 GeV/c beam momentum: Discussion

G. Barr[5], O. Chvala[6], H.G. Fischer[4,a], M. Kreps[1], M. Makariev[7], C. Pattison[5], A. Rybicki[3], D. Varga[4,2], S. Wenig[4,b]

[1] Comenius University, Bratislava, Slovakia
[2] Eötvös Loránt University, Budapest, Hungary
[3] The H. Niewodniczański Institute of Nuclear Physics, Polish Academy of Sciences, Cracow, Poland
[4] CERN, Geneva, Switzerland
[5] Oxford University, Oxford, UK
[6] Charles University, Faculty of Mathematics and Physics, Institute of Particle and Nuclear Physics, Prague, Czech Republic
[7] Atomic Physics Department, Sofia University St. Kliment Ohridski, Sofia, Bulgaria

Received: 14 June 2006 / Revised version: 25 October 2006 /
Published online: 27 January 2007 –

Abstract. The new data on pion production in p+C interactions from the NA49 experiment at the CERN SPS are used for a detailed study of hadronization in the collision of protons with light nuclei. The comparison to the extensive set of data from p+p collisions obtained with the same detector allows for the separation and extraction of the projectile and target contributions to the pion yield both in longitudinal and in transverse momentum.

1 Introduction

Hadron-nucleus interactions constitute a unique laboratory for the study of hadronization in the non-perturbative sector of QCD by offering, in particular, access to multiple hadronic collision processes and by opening an important link to nucleus-nucleus reactions. In fact the latter process cannot be understood properly without reference to the more elementary hadron-hadron and hadron-nucleus interactions. Past attempts in this field have been largely frustrated by the absence of detailed and consistent data sets both from hadron-hadron and from hadron-nucleus collisions. The NA49 experiment aims at providing such data sets obtained with the same detector over a wide range of projectile and target combinations [1] by measuring yields of identified secondaries with a dense coverage of the available phase space.

A recent publication concerning pion production in p+p collisions [2] has now been followed by data of similar quality from minimum-bias p+C interactions [3]. This allows for a new attempt at comparing both reactions and extracting quantitative information about hadronization involving light nuclei. The hadronization process in hadron–nucleus interactions consists of three distinct components:

– The projectile fragmentation which carries the imprint of multiple collisions in nuclear matter and is the part of principle interest for this study.
– The fragmentation of the participating target nucleons.
– The contribution from intranuclear cascading which is generated by the propagation and interaction of the participating nucleons and produced hadrons inside the nucleus.

The separation of the three components is non-trivial if it is to be conducted in a model-independent way. It has been demonstrated by NA49 for the first time in p+Pb collisions concerning net proton production [1]. In this case the full range of projectile and target combinations available to the experiment has been used, with baryon number conservation as the only external constraint.

For pions the situation is more complex as there is no conservation law (except charge conservation) to be exploited. In addition the target cascading part extends closer to the central region than for protons, up to x_F values of about -0.05. Both the target and the projectile components feed-over into the respective opposite hemispheres with a priori unknown ranges and shapes of the longitudinal momentum distributions. These parameters should be determined experimentally without taking recourse to unfounded model assumptions.

The present study will attempt the quantification and separation of the relevant components, with a special view to the extraction of the projectile contribution in its longitudinal and transverse momentum behaviour. For this aim the reference to the elementary hadron–proton interactions is absolutely essential and most of the argumentation will be established in direct compari-

[a] e-mail: Hans.Gerhard.Fischer@cern.ch
[b] e-mail: Siegfried.Wenig@cern.ch

son to these processes, invoking isospin symmetry as an important constraint for the constitution of the target contribution.

In its first part the paper deals with p_T integrated x_F distributions since the superposition process is to first order a matter of longitudinal momentum space. After a presentation of the longitudinal pion yields in relation to p+p collisions in Sect. 2, constraints on the overlap of target and projectile components from elementary interactions are developed in Sect. 3, resulting in a two-component picture of these collisions. This two-component picture is applied to the p+C reaction in Sect. 4 which provides detailed information about the target and projectile fragmentation. Nuclear aspects are discussed in Sect. 5, followed by the quantification of the cascading contribution in Sect. 6. This allows for the extraction of the multiple collision part of the interaction for a number of typical observables, and a comparison to the centrality-constrained data available from the experiment in Sect. 7.

In its second part the paper will exploit the more detailed behaviour of double inclusive cross sections which give access to the study of transverse momentum behaviour. Section 8 presents the general p_T dependencies in relation to p+p interactions and Sect. 9 addresses in particular the behaviour towards higher p_T up to about 1.8 GeV/c. A discussion of the mass and p_T dependence of the feed-over mechanism in relation to resonance decay will close the paper in Sect. 10.

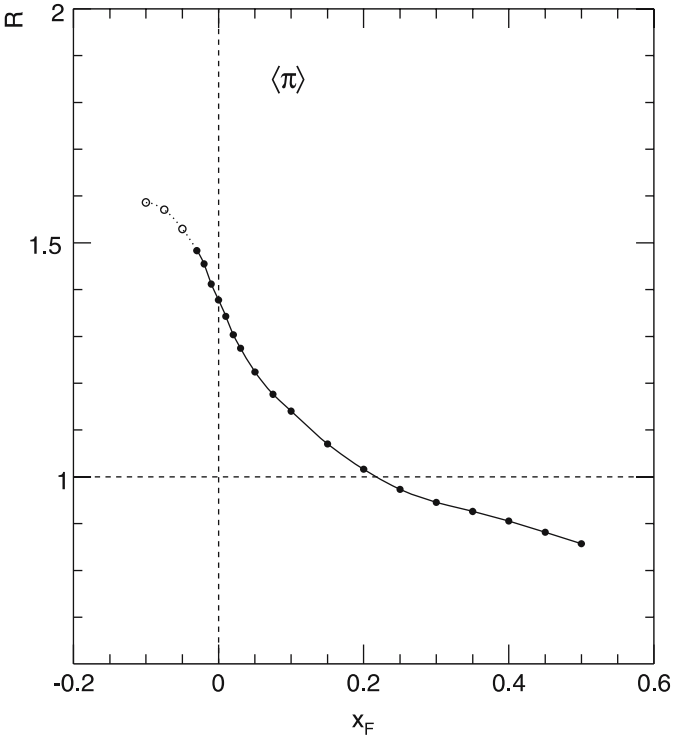

Fig. 1. Ratio $R(x_F)$ as a function of x_F for the charge-average pion $\langle\pi\rangle$. The data points concerned by an extrapolation of the low p_T region are given as open circles

2 p_T integrated x_F distributions: Comparison to p+p interactions

2.1 Charge-average x_F distributions

The most general reduction of the multiparticle phase space of pion production that may be obtained is the p_T integrated, charge-averaged ($\langle\pi\rangle = (\pi^+ + \pi^-)/2$) longitudinal momentum distribution, in the following characterized by the scaling variable

$$x_F = \frac{p_L}{\sqrt{s}/2}, \tag{1}$$

where p_L and $\sqrt{s}$ are given in the nucleon-nucleon cms. This distribution is compared to the p+p interaction [2] by forming the ratio

$$R(x_F) = \frac{(\mathrm{d}n/\mathrm{d}x_F)^{pC}}{(\mathrm{d}n/\mathrm{d}x_F)^{pp}} \tag{2}$$

and shown in Fig. 1. Here the integrated pion densities $\mathrm{d}n/\mathrm{d}x_F$ are obtained from the interpolated double differential cross sections as described in detail in [2] and [3].

Since the acceptance for particle identification of the NA49 detector imposes a limit [3] at $x_F = -0.03$ for the complete integration of the p_T distributions, a slight extrapolation concerning the lowest p_T range of the integration, to $x_F = -0.1$ is also indicated in Fig. 1. This extrapolation uses an extension of the data interpolation developed for the p+C data [3] into the non-measured region of p_T. It is based on the assumption that R should be described by an isoscalar superposition of the proton–nucleon cross section in the target fragmentation region as quantified in Sect. 8. It will be justified in successive steps following the line of argumentation throughout this paper. The data points concerned are given as open circles in Fig. 1. The upper limit of the comparison at $x_F = 0.5$ is due to the limited event statistics in the p+C data sample.

Several features of interest emerge from this first comparison. The ratio R decreases smoothly from about 1.6 at the limit of $x_F = -0.1$ via 1.38 at $x_F = 0$ to a value of 0.85 at $x_F = 0.5$. The factor 1.6 is close to the expected mean number of projectile collisions $\langle\nu\rangle$ inside the carbon–nucleus (see Sect. 5) and the value 1.38 at $x_F = 0$ is close to the expectation $(\langle\nu\rangle + 1)/2$ from the most straightforward projectile-target superposition scheme [4]. The decrease of particle density in the far forward direction recalls a known phenomenon of projectile fragmentation. It corresponds to the x_F dependence of the exponent α in the parametrization:

$$\frac{\mathrm{d}\sigma}{\mathrm{d}x_F} \sim A^{\alpha}, \tag{3}$$

where A is the nuclear weight. For a limited range in transverse momentum and for the far forward direction α has been shown to decrease as a function of x_F [5].

The increased particle density in the region $-0.1 < x_F < 0.2$ on the other hand is due to the superposition of the two principle components of the hadronization process,

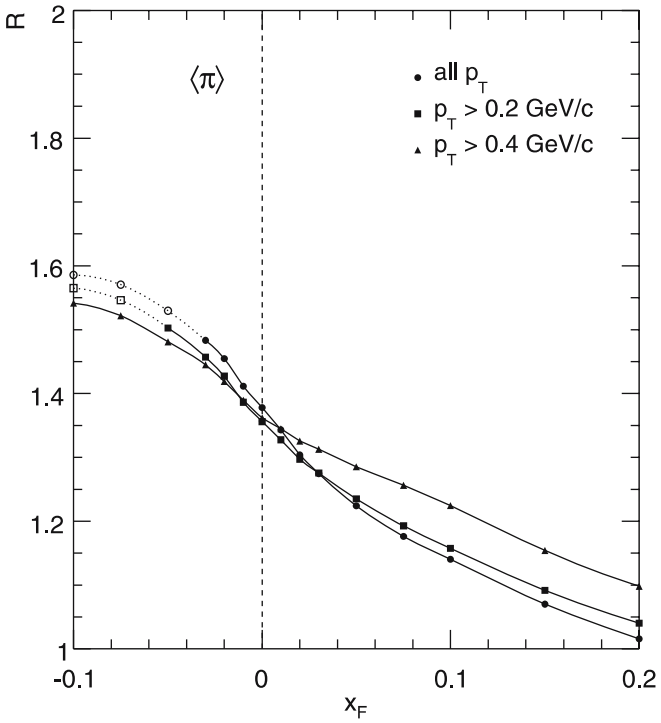

Fig. 2. Ratio $R(x_\mathrm{F})$ as a function of x_F for the charge-average pion $\langle\pi\rangle$ obtained with lower integration limits at $p_\mathrm{T} = 0$, 0.2 and 0.4 GeV/c. The data points concerned by an extrapolation of the low p_T region are given as open symbols

namely the target nucleons participating in the collision and the projectile itself. The quantification and extraction of these two basic ingredients to the p+A interaction is the main aim of this study which can for the first time make full use of the important transition region between the two components. This transition region will be shown to be located between the limits $-0.1 < x_\mathrm{F} < 0.1$.

A first indication concerning the validity of the extrapolation towards $x_\mathrm{F} = -0.1$ used in Fig. 1 is obtained by studying the sensitivity of the integrated yields to a lower cut-off in p_T as shown in Fig. 2.

Here the ratio $R(x_\mathrm{F})$ is obtained for lower integration limits at $p_\mathrm{T} = 0$, 0.2 and 0.4 GeV/c. For the latter value the full region down to $x_\mathrm{F} = -0.1$ is experimentally available. It appears that the effect of the successively increasing cut-offs is on the few percent level for negative x_F and can therefore be considered as a second order phenomenon. It finds its explanation in the p_T dependence of the range in x_F of the projectile feed-over as discussed in Sect. 9. The quantitatively larger effect in the forward hemisphere is noteworthy. It has its origin in the sizeable increase in $\langle p_\mathrm{T}\rangle$ for p+C compared to p+p interactions with ultimately very important p_T dependencies in the range $p_\mathrm{T} > 1.5$ GeV/c (Sect. 8).

2.2 Charge dependence

The yield ratio $R(x_\mathrm{F})$ is plotted separately for π^+ and π^- secondaries in Fig. 3. Evidently there are differences both in the far forward, the projectile hemisphere, and more pronounced, in the backward region. The former effect results in a sizeable increase of the π^+/π^- ratio for $x_\mathrm{F} > 0.3$ and signals an important modification of the projectile fragmentation mechanism. The latter effect is directly related to the target. Due to isospin symmetry [6] the neutron content of the carbon nucleus enhances the π^- and suppresses the π^+ yields from the target relative to the p+p interaction. The observation of the π^+/π^- ratio in this region can therefore provide direct, model-independent access to the relative target contribution.

The ratio R for different lower cut-offs in the p_T integration is also shown in Fig. 3. For π^+ a local maximum of R at $x_\mathrm{F} \sim -0.05$ is followed by a decrease towards lower x_F. For π^- on the other hand a steady increase of R through the same region of x_F is observed. These effects will be studied quantitatively in Sect. 4.

2.3 Charge ratios

The effects discussed above result in a strong backward–forward asymmetry of the charge ratio

$$R_\mathrm{c}(x_\mathrm{F}) = \frac{(\mathrm{d}n/\mathrm{d}x_\mathrm{F})^{\pi^+}(x_\mathrm{F})}{(\mathrm{d}n/\mathrm{d}x_\mathrm{F})^{\pi^-}(x_\mathrm{F})} \qquad (4)$$

for the p+C interaction as compared to p+p. This is demonstrated in Fig. 4 which shows R_c for both the p+C and the p+p reaction as a function of x_F. An enlarged view of the central and backward x_F regions is also presented in Fig. 4 for different p_T cut-offs in the transverse momentum integration, giving further support to the extrapolation used at low p_T.

Again invoking isospin symmetry, an approach of R_c to unity will indicate the region of prevailing target fragmentation, whereas an approach to the values measured in p+p collisions will signal the prevalence of projectile fragmentation. Indeed the plots of Fig. 4 allow to argue that both expectations are fulfilled in the regions $x_\mathrm{F} < -0.1$ and $x_\mathrm{F} > +0.1$, respectively. The situation is, however, more complex in detail. The approach to $R_\mathrm{c} = 1$ is not smooth but shows structure with a local maximum at $x_\mathrm{F} \sim -0.05$, and the R_c values for positive x_F approach but do not quite reach the ones measured in p+p collisions below $x_\mathrm{F} = 0.2$. For $x_\mathrm{F} > 0.3$ on the other hand, they start to exceed these values. A more detailed discussion of these second-order effects will be given in Sect. 4 below.

3 Projectile and target contributions in elementary interactions

The superposition and separation of the target and projectile components in p+A collisions is a main ingredient for the argumentation of this paper. The inspection of these two components also in the elementary hadron–proton interactions is therefore a necessary condition for the model-

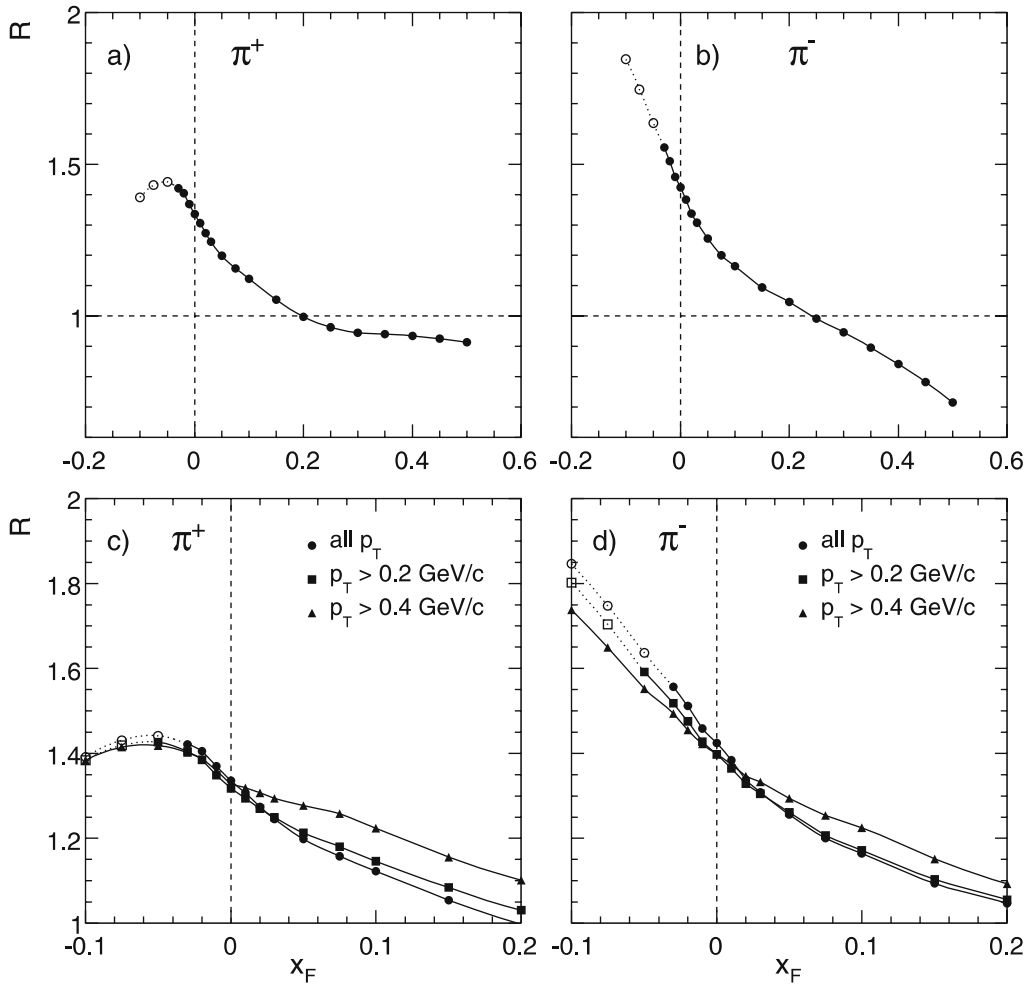

Fig. 3. Ratio $R(x_{\mathrm{F}})$ as a function of x_{F} without p_{T} cut-off (two *upper panels*) and with p_{T} cut-off included (two *lower panels*) for **a** and **c** π^+, **b** and **d** π^-. The data points concerned by an extrapolation of the low p_{T} region are given as *open symbols*

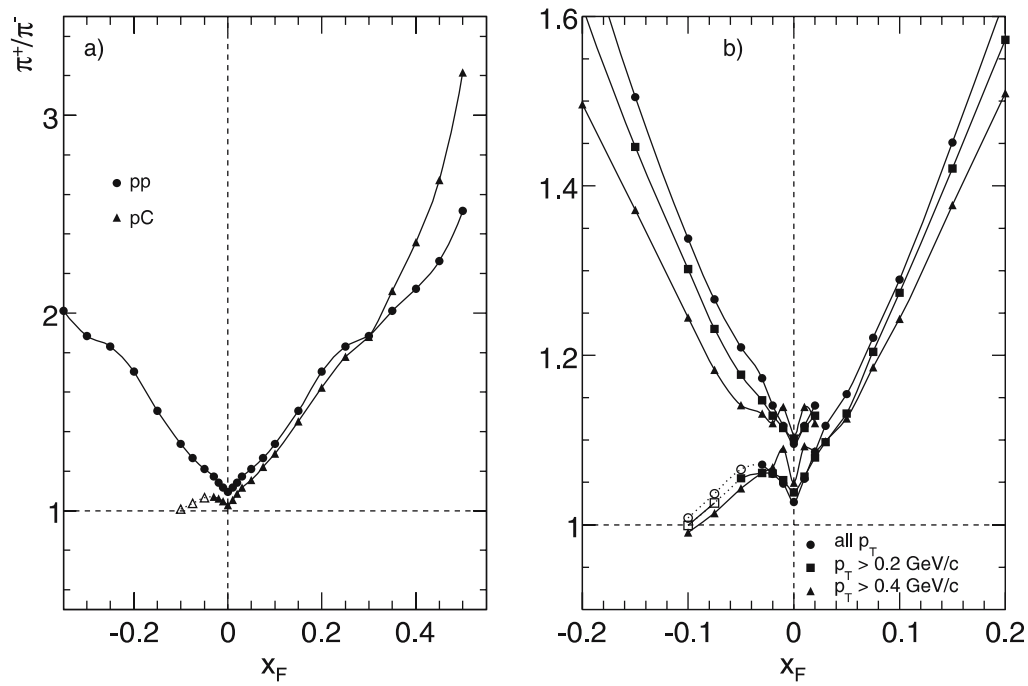

Fig. 4. p_{T} integrated π^+/π^- ratio as a function of x_{F} in p+p and p+C **a** without p_{T} cut-off and **b** with p_{T} cut-off included as the data points in p+p collisions are plotted only up to $x_{\mathrm{F}} = 0.02$. The data points concerned by an extrapolation of the low p_{T} region are given as *open symbols*

independent interpretation of the data. The discussion will be built around three experimental facts:

- The absence of long-range two-particle correlations at $|x_F| > 0.2$.
- The presence of forward–backward multiplicity correlations at $|x_F| < 0.1$.
- The x_F dependence of the π^+/π^- ratio in $\langle\pi\rangle + p$ collisions.

3.1 Long-range two-particle correlations

A high precision study of the forward–backward correlation function

$$Q(x_1, x_2) = \frac{g(x_1, x_2)}{f(x_1) \cdot f(x_2)} \sigma_{\text{trig}} \tag{5}$$

has been performed at the CERN ISR [7] for different combinations of identified secondary hadrons in p+p interactions. Here x_1 and x_2 are the Feynman x values of the two particles which are selected in the opposite hemispheres of the reaction and f and g denote the invariant one and two-particle cross sections, respectively. Typical plots of $Q(x_1, x_2)$ are shown in Fig. 5 for pion pairs and for Kπ and pπ combinations.

The acceptance and particle identification constraints for the two spectrometer arms of the ISR experiment limit the longitudinal coverage to $|x_F| > 0.2$ for pions and $|x_F| > 0.4$ for protons and kaons. Within these limits, no deviation of $Q(x_1, x_2)$ from unity is visible within tight error bars with the only exception of the regions of large x_F where

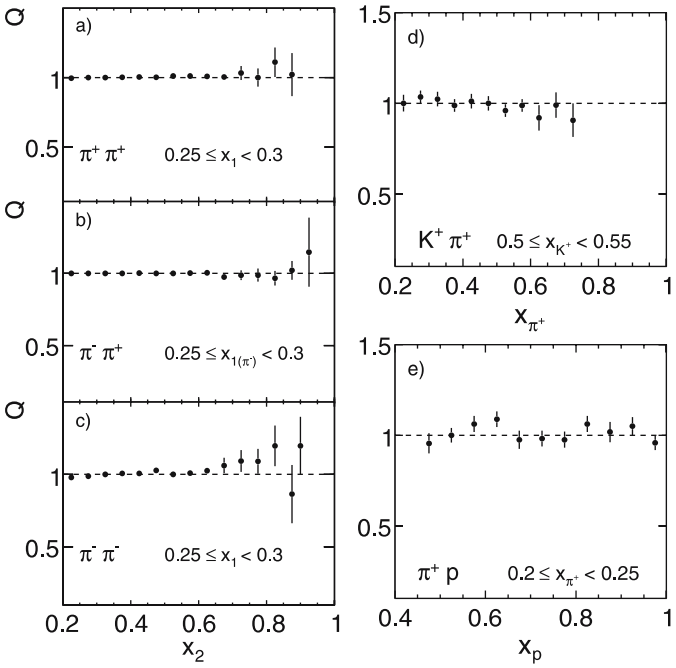

Fig. 5. Forward–backward correlations in p+p collisions measured by [7] for: **a** $\pi^+\pi^+$, **b** $\pi^-\pi^+$, **c** $\pi^-\pi^-$, **d** $K^+\pi^+$, and **e** π^+p

energy-momentum conservation will finally impose some correlations of kinematic origin [7]. Some of the important results of this experiment concern the absence of charge or flavour exchange, the indication of gluon exchange as the exclusive exchange mechanism in soft hadronic collisions at the SPS/ISR energy, and the proof that no notable forward–backward correlations exist above the limit of $|x_F| = 0.2$.

3.2 Forward–backward multiplicity correlations

A series of bubble chamber experiments [8–10] at SPS energies, and a streamer chamber experiment at the ISR [11] have extended the study of [7] to full phase space by establishing multiplicity correlations between the forward and the backward hemisphere. In experiments [8–10] the complete x_F region is accessible by momentum measurement in the fixed-target laboratory frame. Since there is no particle identification available, the assumption of pion mass for the necessary Lorentz transformation creates a certain but practically negligible bias in the determination of central rapidity. Experiment [11] has no momentum measurement and only determines pseudo-rapidity η but the $\eta = 0$ reference is uniquely given for all particles by the angle measurement alone due to the collider geometry of the ISR.

Forward–backward multiplicity correlations are quantified by splitting the charged multiplicity n_{ch} per event into a forward (n_f) and backward (n_b) sample around $y = 0$ or $\eta = 0$ and by plotting the average backward multiplicity $\langle n_b \rangle$ as a function of n_f as shown in Fig. 6.

Except for some odd-even fluctuations at small multiplicities, a linear correlation of the type

$$\langle n_b \rangle = a + b \cdot n_f \tag{6}$$

emerges for all experiments, with values of the slope parameter b between 0.17 and 0.22 in the $\sqrt{s}$ range from 14 to 24 GeV (Fig. 6 a–d). These results do not contradict the absence of correlations shown by [7] above. In fact the observed multiplicity correlations vanish if only particles above one unit of rapidity or pseudo-rapidity are allowed to contribute to the sample, as presented in Fig. 6 f–h. For the region of $\sqrt{s}$ covered and for transverse momenta in the neighbourhood of $\langle p_T \rangle$ this corresponds to a cut in x_F between 0.04 and 0.06 units as shown in Fig. 6 e. This limit is well below the x_F acceptance of [7].

The combined results of Sects. 3.1 and 3.2 allow the statement that in the SPS energy range there is a limited feed-over of (mostly) pion production from the forward to the backward hemisphere and vice-versa. This feed-over contains between 17% and 21% of the particles produced in each hemisphere and is limited to the region of $|x_F| \lesssim 0.05$. There is no further long-range correlation beyond this limit. This statement has to be seen within the experimental uncertainties of Fig. 6 f–h. A tail of feed-over up to $x_F \sim 0.1$ as it is following from the study of charge ratios, Sect. 3.3, will correspond to a percent effect

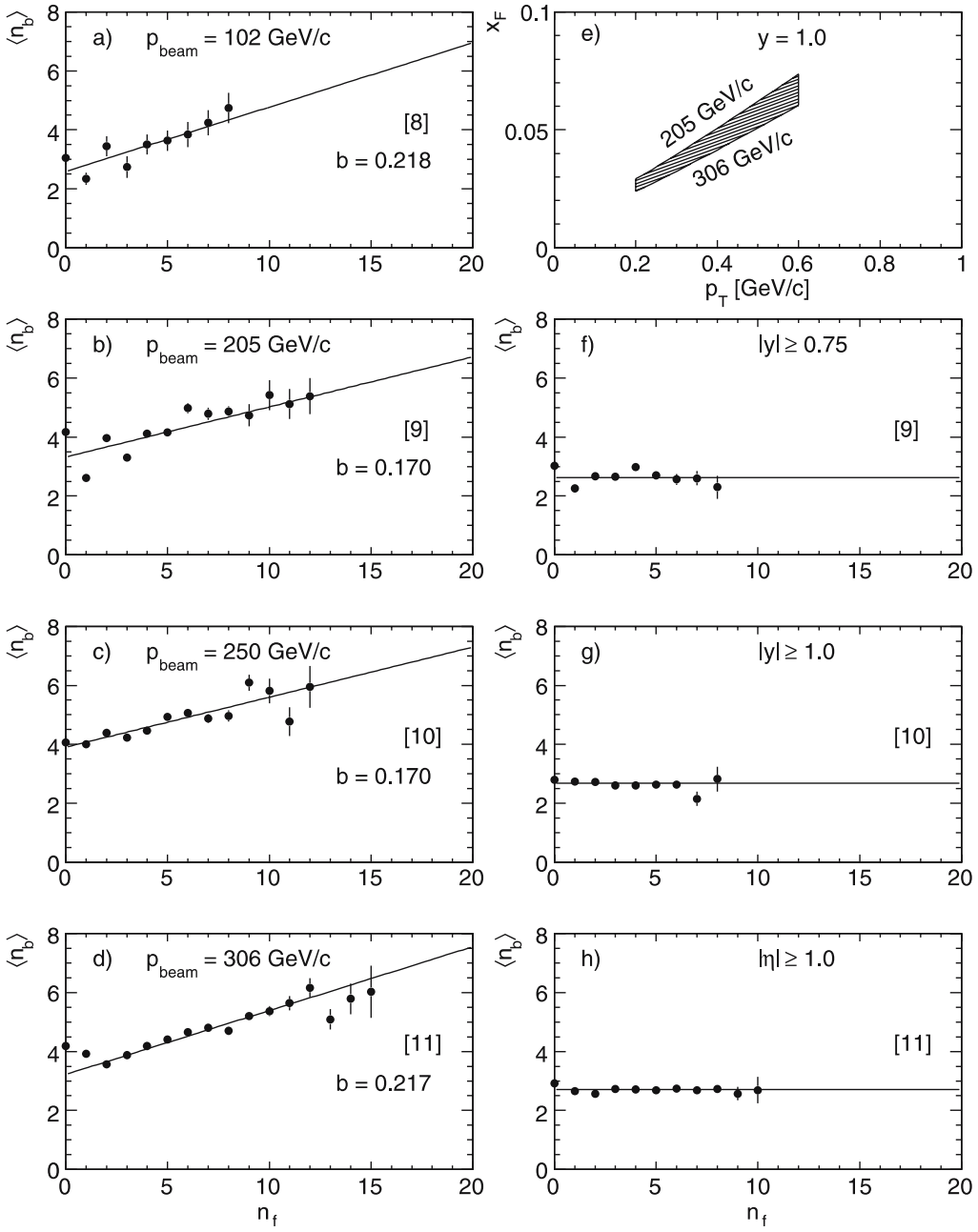

Fig. 6. Forward–backward multiplicity correlations, **a**–**d** experimental data and fits, [8–11]; **f**–**h** correlation with rapidity selection as given, [9–11]; **d** x_{F} as a function of p_{T} at $y = 1$ for beam momentum between 205 and 306 GeV/c

on the slope parameter b and is compatible with the error bars.

Before coming to a further quantification of this situation it is worth while commenting on the energy dependence of the correlation determined by [11]. In fact the correlation factor b increases steadily with $\sqrt{s}$ and reaches a value of $b = 0.31$ at $\sqrt{s} = 62$ GeV. It has been established [11] that this increase is not accompanied by an extension of the feed-over range in x_{F} by showing that the correlation vanishes by replacing the cut at $|\eta| > 1$ by an s-dependent one at $|\eta| > 0.5 \ln s - 2$. This cut happens to correspond in first order to an s-independent x_{F} cut at 0.05. The increase in the correlation is therefore due to the non-scaling increase of central pion production characterized by the rising "rapidity plateau" [12].

3.3 π^+/π^- ratio in pion-induced interactions

The range and shape of the feed-over components of hadronic interactions can also be constrained by using asymmetric collisions and by exploiting a measured quantity that exhibits a predicted behaviour for either the projectile or the target fragmentation.

Such a combination is given by using the π^+/π^- ratio for $\langle\pi\rangle$+p interactions. Here $\langle\pi\rangle$+p indicates the average of π^++p and π^-+p collisions. In this case, the π^+/π^- ratio is exactly unity for the complete projectile fragmentation. This follows in a completely model-independent way from the fulfillment of isospin symmetry in hadronic collisions. By plotting the π^+/π^- ratio as a function of x_{F} one therefore obtains directly the extent and shape of the proton

target feed-over into the projectile hemisphere using the deviation of the measured charge ratio from unity.

Experimentally this means the performance of precision measurements of identified pion yields in the central region both with π^+ and π^- beams. This has been achieved with the NA49 detector [1]. It has been shown that isospin symmetry, i. e. the inversion of π^+ and π^- yields when passing from a π^+ to a π^- projectile, is indeed fulfilled for $x_F > 0.1$ in this reaction [6].

In the determination of the π^+/π^- ratio all experimental corrections drop with the exception of the feed-down from weak decays of strange particles for the proton target contribution. This feed-down which is in principle asymmetric in its π^+ and π^- yields has been quantified. It contributes less than 0.5% to the π^+/π^- ratio in the forward region and has been corrected for.

The resulting pionic charge ratio is shown in Fig. 7 as a function of x_F for $\langle\pi\rangle$+p collisions in comparison to the same quantity in p+p interactions.

For $\langle\pi\rangle$+p the π^+/π^- ratio levels off to unity at x_F above 0.08 and stays constant at this value up to the limit of data extraction at $x_F = 0.3$. The same ratio for p+p collisions shows the known strong increase with x_F [2] which is reflecting the presence of the proton projectile. Surprisingly, the approach of the charge ratio to unity is not smooth but shows a characteristic structure with a secondary maximum at $x_F \sim 0.04$ which is reminiscent of the similar behaviour of this ratio in the target hemisphere of p+C interactions, Fig. 4. It should be emphasized here that the precision of the charge ratio as far as statistical and systematic errors are concerned, is on the sub-percent level in this region.

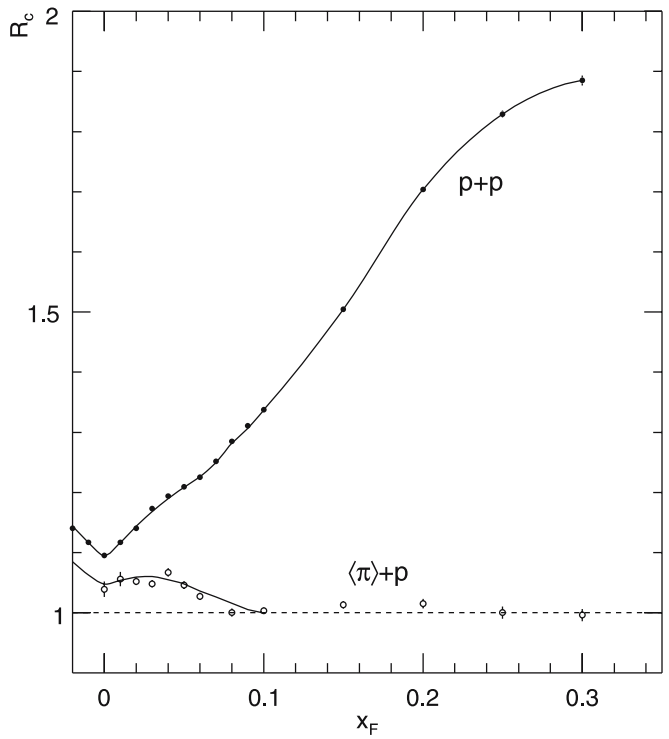

Fig. 7. π^+/π^- ratio in p+p and $\langle\pi\rangle$+p

3.4 A two-component picture of pion production in p+p and $\langle\pi\rangle$+p collisions

The combined experimental evidence collected in the preceding sections allows for the construction of a two-component picture for pion production in elementary hadronic interactions. The two components correspond to the target and the projectile contributions. These contributions obey factorization, a well known phenomenon in hadronic reactions which specifies that the target component is independent of the projectile particle type, and vice-versa for the projectile fragmentation. Both components feed-over into the opposite hemisphere with a range that has a maximum extent of 0.1 units of x_F in the SPS/ISR energy range, Sect. 3.3. Fixing this range, using the symmetry constraint at $x_F = 0$ in p+p collisions and limiting the integral of particle yield in the opposite hemisphere to about 19% of the total yield per component, Sect. 3.2, there is very limited freedom in the construction of this two-component picture. Figure 8 shows the x_F dependence of the two components as it is obtained obeying the above constraints, and their superposition to the measured total inclusive yield for p+p collisions.

The behaviour in the feed-over region $-0.1 < x_F < 0.1$ can be further quantified by plotting the ratio of the proton target component relative to the total inclusive pion yield

$$t(x_F) = \frac{(dn/dx_F)_{\text{target}}}{(dn/dx_F)_{pp}}, \tag{7}$$

as presented in Fig. 9. The corresponding projectile component, $p(x_F)$, is related to $t(x_F)$ by $p(x_F) = t(-x_F)$ for p+p interactions.

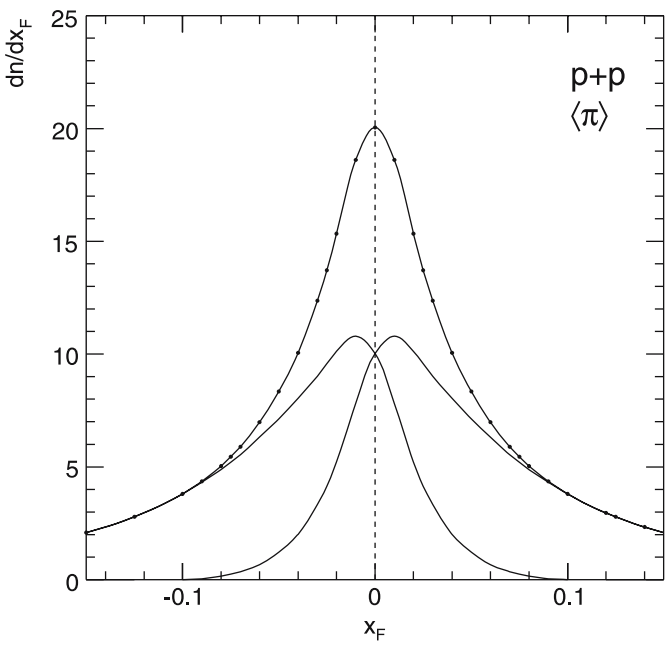

Fig. 8. Two-component picture of charge-averaged pion production in p+p collisions, showing the symmetric contribution from the target and projectile and their sum corresponding to the data [2]

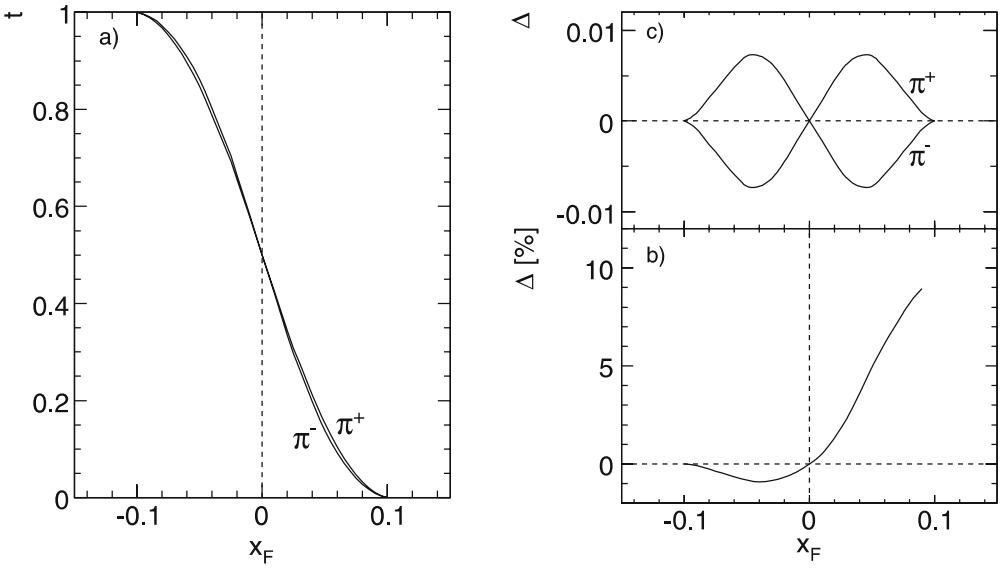

Fig. 9. Target component of π^+ and π^-: **a** absolute value with respect to the total yield, **b** absolute deviation from the target component of $\langle\pi\rangle$, and **c** deviation in percent for π^+

In this figure two slightly different shapes are indicated. They correspond to the two pion charges. This shape difference is necessitated by the structure in the π^+/π^- ratio around $x_F = 0.04$ observed in Fig. 7. In fact there is no a priori knowledge of the behaviour of the two charge states in the feed-over region: they may and indeed do differ from each other. This difference is quantified in Fig. 9 b and c with respect to the charge-average distribution. It corresponds to a decrease followed by a steep increase of the π^+/π^- ratio as one moves from the target hemisphere into the projectile region. This is shown in Fig. 10 which gives the corresponding prediction for the measured π^+/π^- ratio both for p+p and $\langle\pi\rangle$+p collisions.

It is interesting to note that the measurement for both reactions is precisely described, yielding a simultaneous explanation for the slight shoulder and the structure around $x_F = 0.04$ observed in p+p and $\langle\pi\rangle$+p collisions, respectively. This corresponds to a long-range charge correlation within the target and projectile contributions with the respective incoming hadron, which is for the first time extracted here. This correlation will present an interesting challenge for microscopic production models, in particular for those based on string fragmentation ideas, as the memory of the original parton charge tends to be quickly lost along the string [13].

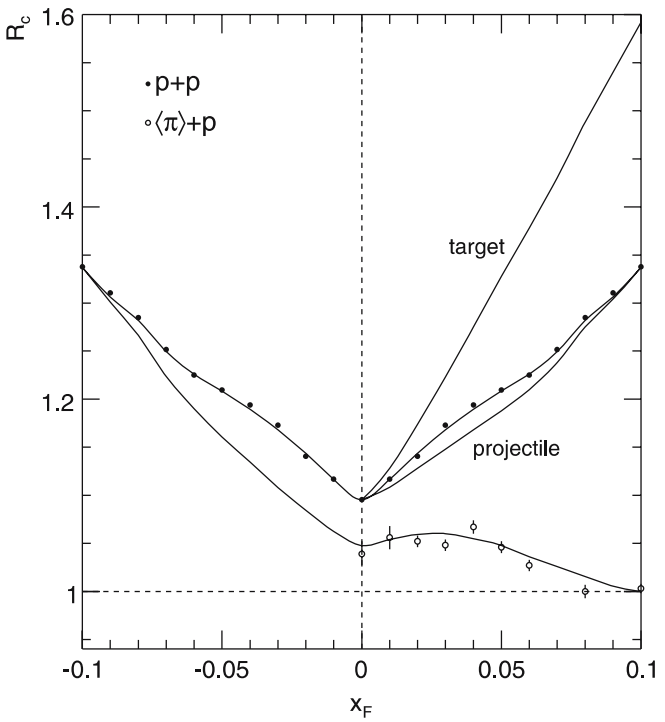

Fig. 10. π^+/π^- ratio in p+p and $\langle\pi\rangle$+p with corresponding predictions for the proton target and proton projectile components

3.5 Comparison to the feed-over in net baryon production

The NA49 data from p+p and $\langle\pi\rangle$+p interactions have been previously used to extract the two-component nature of net baryon production. The method used is different from the one applied for the pion production as net baryon number conservation can be invoked as a powerful constraint. The argumentation gives consistent results using pion induced collisions and the forward–backward baryon correlation in p+p events [14]. The extracted shape of the feed-over distribution is directly and independently measured by three methods in a completely model-independent way. The result is shown in Fig. 11 in comparison to the pion feed-over obtained above.

There is clearly an important difference between net protons and pions concerning the range of the feed-over. This indicates a strong mass dependence. In connection with the yield increase with transverse momentum, Sect. 8, it will be argued that there is also a p_T dependence of the feed-over. Both the mass and the p_T dependence will be shown in Sect. 10 to follow from resonance decay.

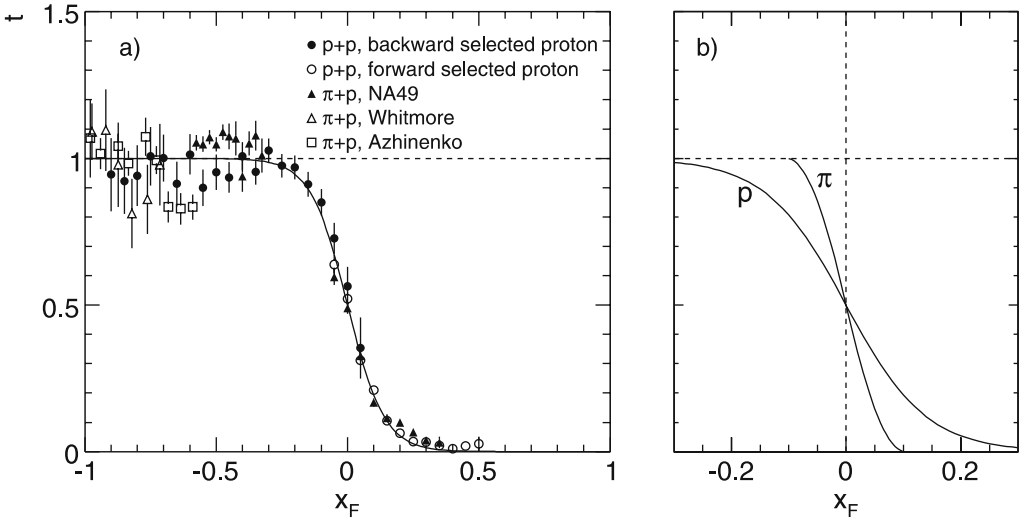

Fig. 11. **a** target component for net protons measured with different methods and **b** target components of $\langle\pi\rangle$ and net protons

4 Projectile and target components in the p+C interaction

4.1 Pion yields

The two-component picture of elementary hadronic collisions developed in the preceding section can now be used to construct the superposition of target and projectile components also for p+C interactions. The third component given by intranuclear cascading will be shown in Sect. 6 below to not contribute in the studied x_{F} range.

Several straight-forward assumptions have to be made in order to quantify this superposition:

- Both the target and the projectile components are assumed to follow the same feed-over mechanism as extracted for the elementary collisions as far as relative shape and x_{F} range are concerned, as shown in Fig. 9.
- In terms of pion yields the target contribution has however a weight $\langle\nu\rangle$ where ν is the number of projectile collisions with the participating target nucleons. The underlying assumption is here that subsequent projectile collisions lead to the same density distribution per participating nucleon.
- In addition and due to the isoscalar nature of the carbon nucleus, the density distribution for both π^+ and π^- is built up as

$$\left(\frac{\mathrm{d}n}{\mathrm{d}x_{\mathrm{F}}}\right)_{\mathrm{target}}(\pi^{\pm}) = \frac{1}{2}\left(\frac{\mathrm{d}n}{\mathrm{d}x_{\mathrm{F}}}\right)^{\mathrm{pp}}_{\mathrm{target}}(\pi^{+}) + \frac{1}{2}\left(\frac{\mathrm{d}n}{\mathrm{d}x_{\mathrm{F}}}\right)^{\mathrm{pp}}_{\mathrm{target}}(\pi^{-}) \quad (8)$$

  which results as necessary in a π^+/π^- ratio of unity over the full x_{F} range.
- The projectile component on the other hand carries the full imprint of $\langle\nu\rangle$ collisions and is as such not predictable. Its model-independent quantification and extraction is the main aim of this section. In a first instance, it is assumed to be identical to the elementary p+p collision,

$$\left(\frac{\mathrm{d}n}{\mathrm{d}x_{\mathrm{F}}}\right)_{\mathrm{proj}}(\pi^{\pm}) = \left(\frac{\mathrm{d}n}{\mathrm{d}x_{\mathrm{F}}}\right)^{\mathrm{pp}}_{\mathrm{proj}}(\pi^{\pm}) \quad (9)$$

  with the aim to extract its real shape by inspecting the deviations of the data from this simple parametrization.

With these assumptions, a prediction for the expected pion density distribution in p+C collisions can be obtained as follows:

$$\left(\frac{\mathrm{d}n}{\mathrm{d}x_{\mathrm{F}}}\right)_{\mathrm{pred}}(x_{\mathrm{F}}) = \langle\nu\rangle\left(\frac{\mathrm{d}n}{\mathrm{d}x_{\mathrm{F}}}\right)_{\mathrm{target}}(x_{\mathrm{F}}) + \left(\frac{\mathrm{d}n}{\mathrm{d}x_{\mathrm{F}}}\right)^{\mathrm{pp}}_{\mathrm{proj}}(x_{\mathrm{F}}) \quad (10)$$

For ease of comparison with the data, see Sect. 2, the prediction is referred to the p+p interaction by forming the ratio

$$R_{\mathrm{pred}}(x_{\mathrm{F}}) = \frac{(\mathrm{d}n/\mathrm{d}x_{\mathrm{F}})_{\mathrm{pred}}(x_{\mathrm{F}})}{(\mathrm{d}n/\mathrm{d}x_{\mathrm{F}})^{\mathrm{pp}}(x_{\mathrm{F}})} \quad (11)$$

This ratio is plotted in Fig. 12 for three different values of $\langle\nu\rangle$ and compared to the measurements as a function of x_{F}.

Several points are noteworthy in this comparison:

- A fair description of the data is obtained in the backward hemisphere at x_{F} towards -0.1 for the value $\langle\nu\rangle = 1.6$. The sensitivity of the comparison to $\langle\nu\rangle$ is clearly evident from the Fig. 12.
- This holds simultaneously for the average pion yield and for the π^+ and π^- yields separately, both in size and in local slope.
- This is a strong indication for the validity of the two-component picture in this region where the target contribution alone should determine the total yields for $x_{\mathrm{F}} = -0.1$ and below.
- Moving from this x_{F} value towards the forward region, the measurements exceed R_{pred} up to $x_{\mathrm{F}} \sim 0.2$ in a characteristic fashion.
- For $x_{\mathrm{F}} > 0.2$ the data fall below the predicted values R_{pred}.

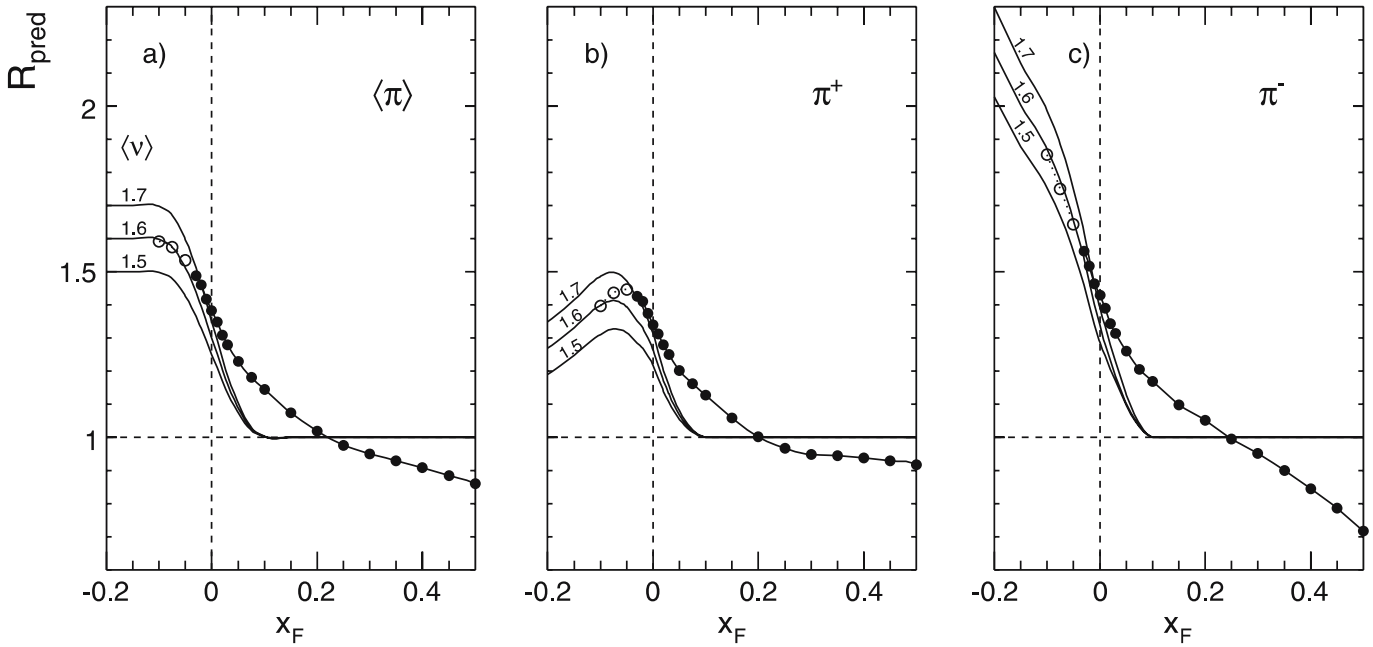

Fig. 12. $R_{\rm pred}$ for different $\langle\nu\rangle$ compared to the measurement (*circles*) for **a** $\langle\pi\rangle$, **b** π^+, and **c** π^-; the data points, $R(x_{\rm F}) = ({\rm d}n/{\rm d}x_{\rm F})^{\rm pC}/({\rm d}n/{\rm d}x_{\rm F})^{\rm pp}$ are also given. The data with fully measured $p_{\rm T}$ range are given as *full circles*, the data using partial extrapolation with *open circles*

The deviation from $R_{\rm pred}$ can be translated into absolute particle densities as shown in Fig. 13 as a function of $x_{\rm F}$.

The obtained density difference follows the shape of the projectile contributions in p+p collisions up to $x_{\rm F} \sim 0.1$. This is shown in Fig. 14 where the difference $\Delta({\rm d}n/{\rm d}x_{\rm F})$ is superimposed to the projectile charge density distribution for $\langle\pi\rangle$, see Fig. 8. The fact that this excess of pion density has the same shape as the projectile component proper in p+p collisions may be regarded as a further strong indication that the two-component superposition picture produces indeed a valid description of the data. The region of reduced particle density at $x_{\rm F} > 0.2$ contributes as expected only a very small negative contribution to the absolute increase of pion density. Integrating the density differences of Fig. 13 it emerges that the projectile pion yields are enhanced by about 10% with respect to p+p collisions [2]. It should be pointed out that such an increase is quite a large effect, account taken of the small difference between $\langle\nu\rangle = 1$ in p+p and $\langle\nu\rangle = 1.6$ in p+C collisions. This carries interesting consequences for the interpretation of the corresponding increase of pion production observed in central nucleus–nucleus interactions, where the

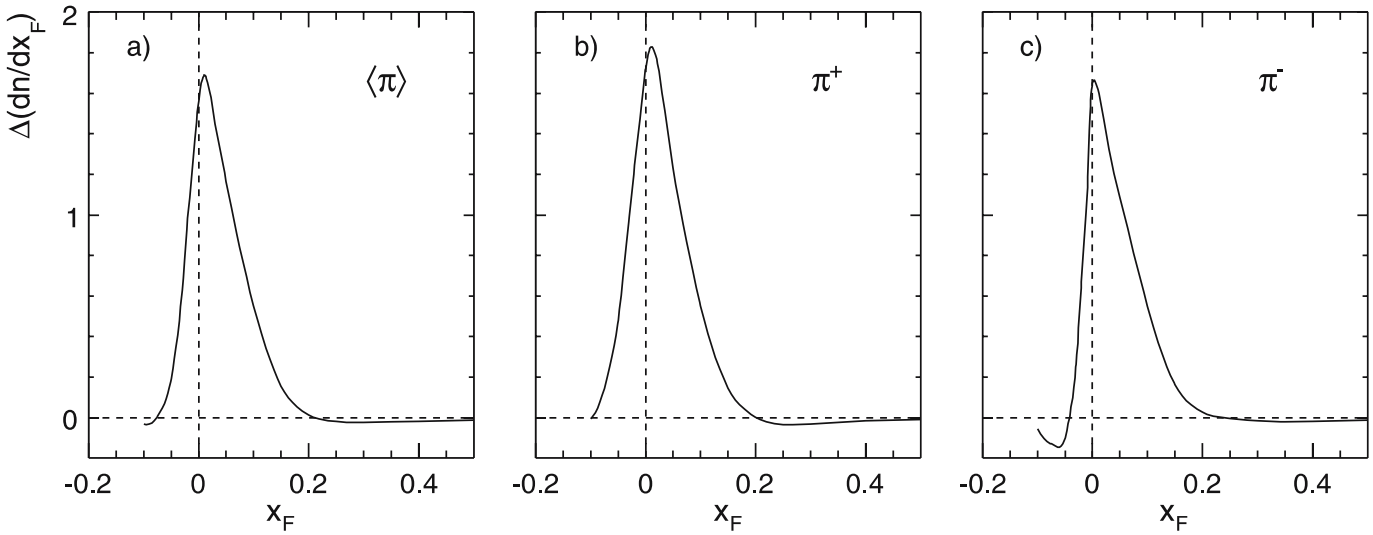

Fig. 13. Difference between measured ratio and predicted yield for **a** $\langle\pi\rangle$, **b** π^+, and **c** π^- for $\langle\nu\rangle = 1.6$

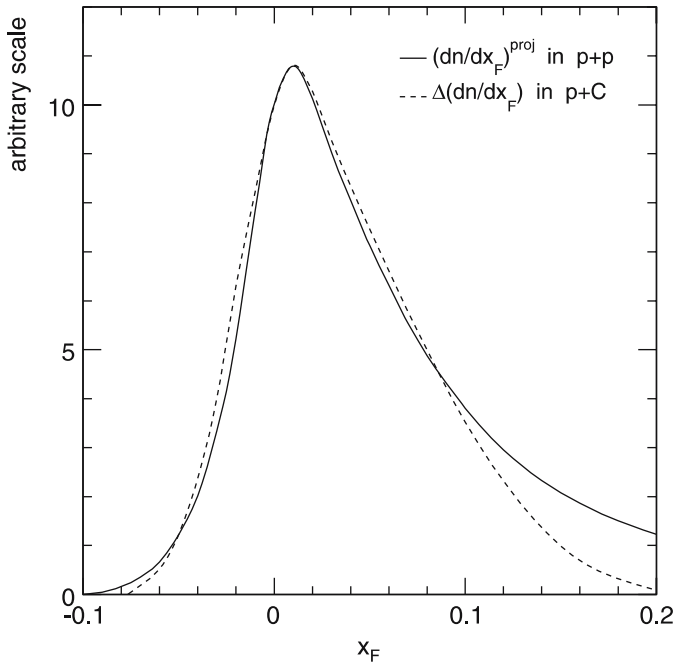

Fig. 14. Shape comparison of the x_{F} distribution of $\Delta(\mathrm{d}n/\mathrm{d}x_{\mathrm{F}})$ in p+C (*dashed line*) and the projectile component $(\mathrm{d}n/\mathrm{d}x_{\mathrm{F}})_{\mathrm{proj}}$ in p+p collisions (*full line*)

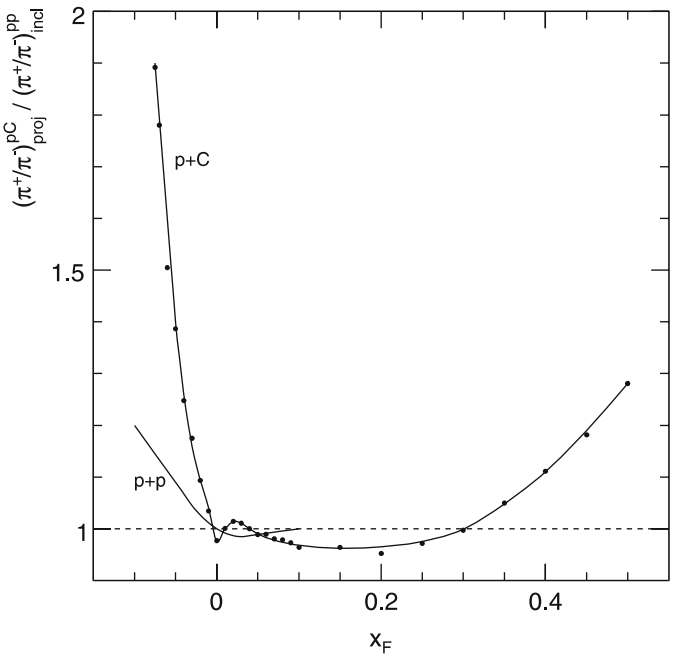

Fig. 15. Charge ratio of the projectile component in p+C divided by the inclusive ratio in p+p collisions. The analogous ratio in p+p collisions is shown for comparison

enhancement does not exceed 30%–40% [15], while all the participating nucleons undergo $\langle\nu\rangle = 4.6$ collisions.

4.2 Charge ratios

The investigation of the π^+/π^- ratio offers an additional and very sensitive tool for the scrutiny of the target-projectile superposition mechanism. As already shown in Sect. 2, Fig. 4, the overall behaviour of the charge ratio complies with the expectation from a two-component picture in the sense that unity is approached in the region of prevailing target contribution, $x_{\mathrm{F}} < -0.1$, and the π^+/π^- ratio observed in p+p collisions is approached in the projectile fragmentation region, $x_{\mathrm{F}} > 0.1$. There are, however, detailed deviations from this first-order expectation. The approach to unity at negative x_{F} is not smooth but resembles the structure observed in $\langle\pi\rangle$+p collisions at $x_{\mathrm{F}} > 0$, i. e. in the corresponding isoscalar projectile fragmentation region of the elementary hadronic reaction. The π^+/π^- ratio of p+p collisions is not quite reached in the forward region below $x_{\mathrm{F}} = 0.3$. These deviations correspond to a modification of the projectile charge ratio in multiple collision processes both in the forward and backward regions. A first indication for the backward hemisphere is contained in Fig. 13 where the density difference for π^+ reaches further out towards negative x_{F} than the one for π^-. This resembles the behaviour already found for the elementary collisions, Sect. 3, Fig. 9.

Using the quantitative superposition scheme developed in the preceding Sect. 4.1 for $\langle\nu\rangle = 1.6$, which explicitly contains the π^+/π^- ratio of unity for the target fragmentation part, the deviation of the projectile charge ratio from the one measured in inclusive p+p collisions may be extracted. It is shown in Fig. 15 as the ratio $(\pi^+/\pi^-)^{\mathrm{pC}}_{\mathrm{proj}}/(\pi^+/\pi^-)^{\mathrm{pp}}_{\mathrm{incl}}$.

Apparently there is again an increase of the charge ratio in the projectile feed-over region. This increase is stronger than the one observed in elementary p+p collisions, Fig. 10, also shown for comparison. It is followed by a decrease of about 4% between $x_{\mathrm{F}} \sim 0.1$ and $x_{\mathrm{F}} \sim 0.25$ and again by an increase at x_{F} beyond 0.3. This represents an interesting feature of the multiple collision process in proton–nucleus collisions in the sense that the projectile charge is correlated to both extremes of the fragmentation region. Due to the small contribution in absolute yield from these areas, the decrease of the charge ratio in the intermediate region is imposed by total charge conservation in view of the increase of projectile multiplicity.

5 Nuclear aspects

Up to this point the discussion was performed without recourse to any details concerning the manifestation of the carbon nucleus. Only its isospin symmetry and the general possibility of multiple projectile collisions were invoked. It is now necessary to come to a more quantitative assessment of a number of nuclear parameters which are essential for the further extension of the argumentation. The decisive quantity for most of the nuclear parameters is the nuclear

density distribution, $\rho(r)$, which determines the rms radius and the probability of single projectile collision, $P(1)$. The second quantity of principle interest is the projectile-nucleon total inelastic cross section, or rather its evolution with subsequent collisions. Only by making very distinct assumptions about this quantity further important parameters like the probability distribution of multiple collisions, $P(\nu)$ and its mean value $\langle\nu\rangle$, already introduced above, may be obtained. The quantitative results on several parameters discussed below come from a detailed Monte Carlo calculation [16] using the density profile as an input.

5.1 Nuclear density distribution and percentage of single collisions

The principle experimental information available for the carbon nucleus comes from electron scattering experiments [17, 18] which measure the nuclear charge distribution. This is not identical with the density profile $\rho(r)$ as the spatial distribution of charge in the proton has to be unfolded. An additional problem resides in the possible asymmetry between proton and neutron distributions. Altogether this leads to a substantial uncertainty about the density profile. Fig. 16 gives $\rho(r)$ for six different parametrizations:

1. Saxon–Woods [19].
2. Single Gaussian [16].
3. Fourier–Bessel [20].
4. Sum of Gaussians [21].
5. Fourier–Bessel unfolded for proton charge distribution [16].
6. Sum of Gaussians unfolded for proton charge distribution [16].

In consequence the rms radius, the nuclear density at the origin and the probability of single collisions (which depends on the elementary proton+nucleon inelastic cross section) show substantial spreads according to the parametrization chosen. This is quantified in the Fig. 16 b–d for the rms radius, the central nucleon density $\rho(r = 0)$, and the probability of single collision $P(1)$. Excluding the first two options which are known to disagree with the experimental evidence, one may conclude on an rms radius between 2.3 and 2.5 fm and on a fraction of single collisions between 0.56 and 0.60. The latter quantity recalls a basic weakness of minimum-bias proton–nucleus experiments given by the fact that a large fraction of events corresponds to "trivial" proton–nucleon collisions. This fraction descends only slowly with increasing atomic number A [16], as shown in Fig. 17.

The contribution of single collisions can in principle be taken out of the experimental results since the percentage $P(1)$ is rather precisely determined and the corresponding target and projectile components can be safely predicted from elementary collisions. This will be demonstrated in the subsequent sections of this paper. An experimentally more efficient way is given by triggering on the presence of "grey" protons [22] already at the level of data taking which has the additional advantage of permitting the control of centrality. Unfortunately, this method could not be applied to the data of [3] due to external constraints on the time available for data taking.

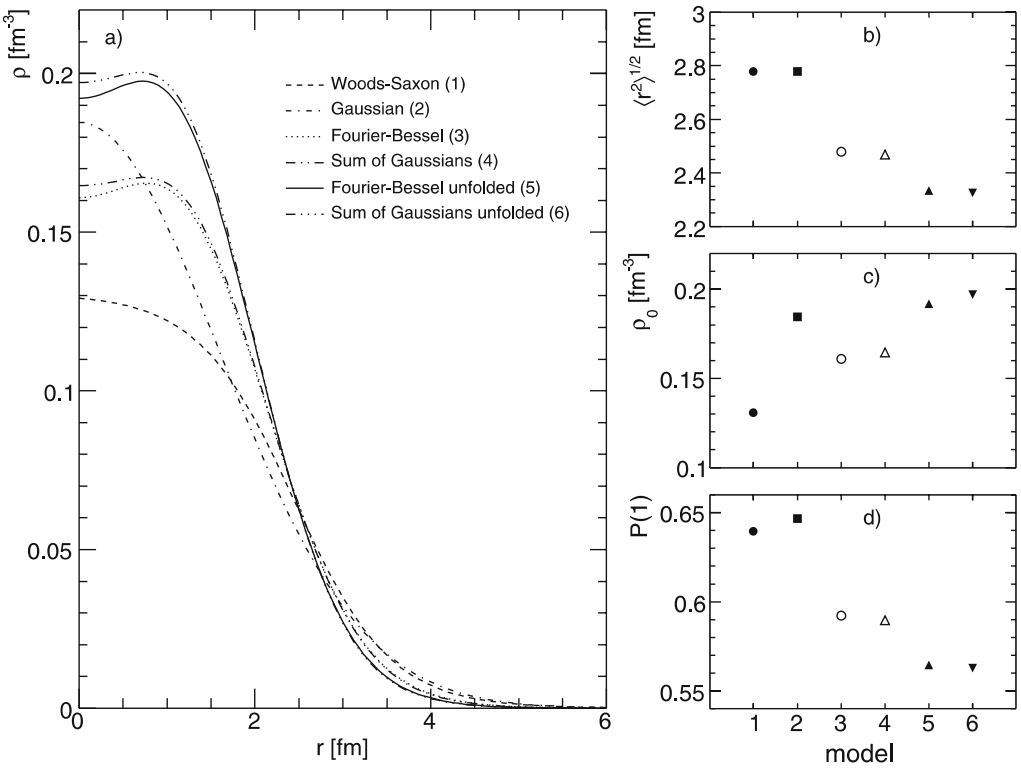

Fig. 16. **a** nuclear density profile parametrizations; **b** rms radius; **c** nuclear density at $r = 0$; **d** probability for single collision

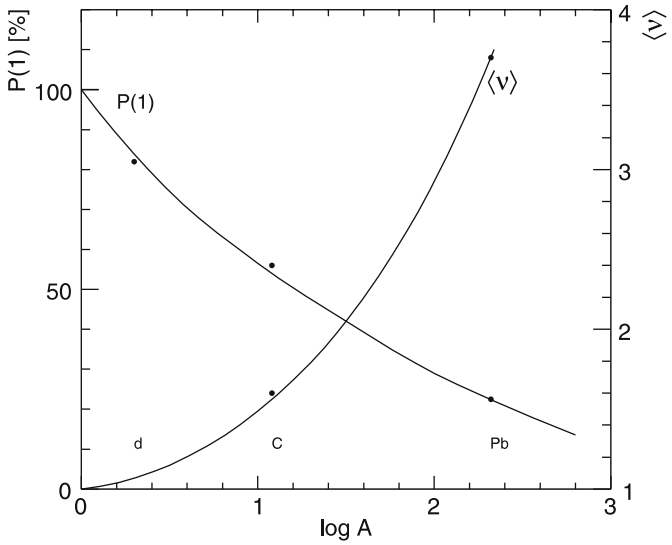

Fig. 17. Probability for single collision and mean number of collisions as a function of atomic number

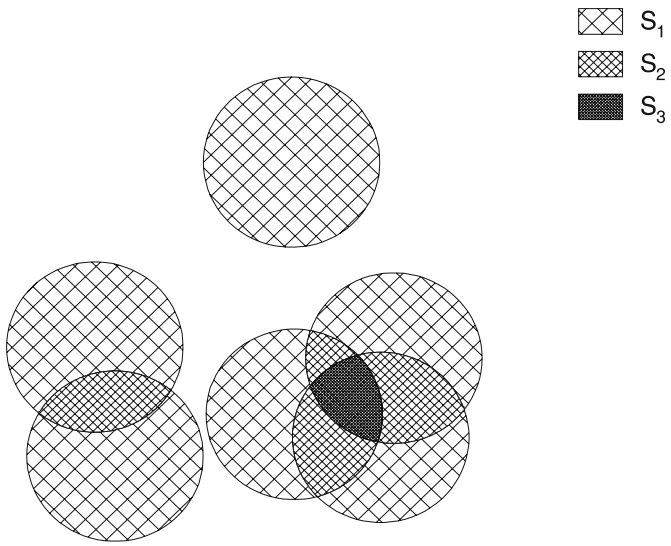

Fig. 18. Schematic view of the superposition of nucleon–nucleon cross sections in a nuclear environment

5.2 The probability distribution of multiple hits and its relation to the total inelastic cross section

Any further specification of nuclear parameters in relation to the interaction of a hadronic projectile with the nucleus has to rely on assumptions on the elementary hadron–nucleon cross section for multiple collisions. The problem may be visualized in a simple geometrical way by looking at a random superposition of A circular disks, each with a surface S of $\sigma^{\mathrm{pp}} = 31.8\,\mathrm{mb}$, as shown in Fig. 18.

The surface area covered by one layer of disks is denoted by S_1. S_2 is the area covered by two layers, S_3 by three layers etc. Scanning the plane with a random distribution of projectiles, the mean hit number of layers will be

$$\langle\nu\rangle = \frac{S_1 + 2S_2 + 3S_3 + \ldots + AS_A}{S_1 + S_2 + S_3 + \ldots + S_A}. \qquad (12)$$

The total area covered by the disks is $S_1 + S_2 + S_3 + \ldots + S_A$. It represents the total inelastic cross section σ^{pA}. The

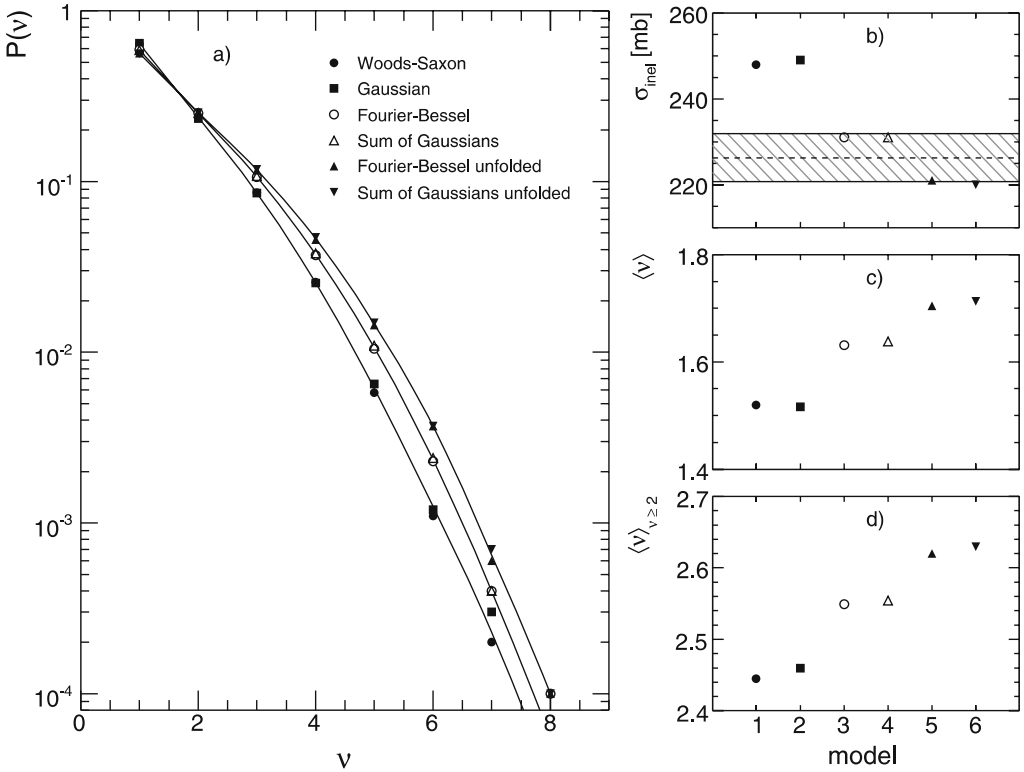

Fig. 19. a Probability of ν collisions for different nuclear density parametrizations; **b** inelastic cross section. The *dashed line* indicates the NA49 result with the error margin (*shaded area*); **c** mean number of collisions; **d** mean number of collisions for $\nu \geq 2$

total surface of the disks, which is $A\sigma^{\mathrm{pp}}$, is given by

$$A\sigma^{\mathrm{pp}} = S_1 + 2S_2 + 3S_3 + \ldots + AS_A. \quad (13)$$

The mean number of collisions is therefore defined by the formula [23]

$$\langle\nu\rangle = \frac{A\sigma^{\mathrm{pp}}}{\sigma^{\mathrm{pA}}}. \quad (14)$$

This formula is clearly only valid if the disk surface describing the inelastic projectile-nucleon cross section is the same in each of the successive layers corresponding to the multiple projectile collisions. Any experimental verification of the mean number of collisions provides therefore an important constraint on the evolution of the cross section with ν.

Always under the above assumption, the distribution $P(\nu)$ of the probability to produce ν collisions in one event, has been determined, using the different nuclear density profiles discussed above, via a Monte Carlo calculation [16]. The result is shown in Fig. 19 which also gives the integrated quantities $\sigma^{\mathrm{pA}}_{\mathrm{inel}}$, $\langle\nu\rangle$ and the mean number of collisions excluding single hits, $\langle\nu\rangle_{\nu\geq 2}$.

In principle the measured value of the inelastic cross section at 226.3 mb $\pm$ 2% (Fig. 19 b) gives a constraint on the nuclear profile and favours the charge-unfolded distributions (5) and (6). This would then correspond to a predicted mean number of collisions of about 1.68. The value of 1.6 extracted from the pion data in the preceding section is indeed close but significantly below this prediction as can be seen from the strong dependence on $\langle\nu\rangle$ of the density ratios shown in Fig. 12.

6 Intranuclear cascading

In the preceding discussion only the principle components of target and projectile fragmentation have been treated. The third contribution to the pion yields due to the propagation and interaction of the participant nucleons and of their fragmentation products inside the nucleus, will now be investigated. The proper Lorentz frame for the description of this intranuclear cascading process is the rest system of the target as the cascading products will have typically small momenta in this system. The kinematic situation is indicated in Fig. 20. Here lines at constant total momentum p_{lab} and constant polar angles Θ_{lab} for pions in the target rest frame are given in the $x_{\mathrm{F}}/p_{\mathrm{T}}$ plane. Pion production is centered at low p_{tot} at $x_{\mathrm{F}} \sim -0.15$, as expected from the mass ratio m_π/m_p. Large values of p_{lab} are needed to approach, at forward production angles, the region close to $x_{\mathrm{F}} = 0$.

The NA49 acceptance is indicated as a hatched area in Fig. 20. It appears that this acceptance matches in its backward low p_{T} part the line at 0.6 GeV/c total momentum. At this momentum the intranuclear pion production yield is already reduced and only small if any cascading contributions are to be expected from this kinematic fact alone. This argument can however be quantified by making

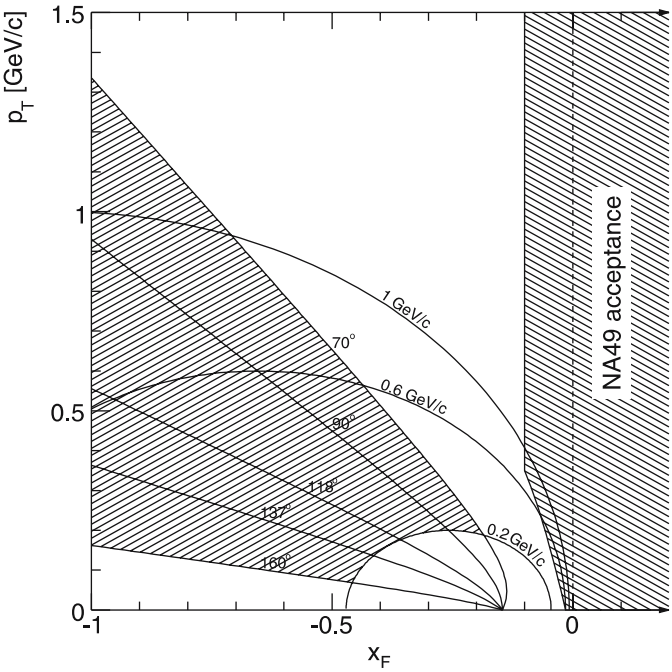

Fig. 20. Kinematic situation in the backward region. With *lines* are indicated the constant total momentum p_{lab} (0.2, 0.6 and 1 GeV/c) and constant polar angle Θ_{lab} (70°, 90°, 118°, 137°, 160°). The *shaded areas* represent the coverage of [24] (far backward region) and NA49 (central and forward region)

use of the measurements of Nikiforov et al. [24] at Fermilab with a beam momentum of 400 GeV/c. This important and unique experiment covers the backward region in the second hatched area indicated in Fig. 20 by measuring identified pion yields at constant Θ_{lab} between 70 and 160 degrees, leaving only a small uncovered zone with respect to the NA49 acceptance. A set of 32 cross sections is available at $x_{\mathrm{F}} > -1.0$ for the assessment of pion yields in p+C interactions.

As the experimental layout of the experiment [24] does not allow a discrimination of off-vertex tracks it must however be expected that the complete feed-down from weak decays of strange particles is contained in the data at these low total momenta. A feed-down correction has therefore been calculated and applied following the methodology developed for the NA49 data [3].

In order to put the Nikiforov et al. data [24] into perspective and to allow for a quantitative comparison, the given cross sections are related to the isospin averaged prediction for the target fragmentation developed and justified in the preceding sections. This is possible since no contribution from projectile hadronization can be expected in the covered area. The ratio

$$R_{\mathrm{casc}} = \frac{(E\mathrm{d}^3\sigma/\mathrm{d}p^3)_{\mathrm{Nikiforov}}}{(E\mathrm{d}^3\sigma/\mathrm{d}p^3)_{\mathrm{pC}}} \quad (15)$$

is plotted in Fig. 21 for the 5 measured angles as a function of p_{T}.

$R_{\rm casc}$ increases strongly with $p_{\rm T}$ for all angles. This is due to the corresponding increase of $|x_{\rm F}|$ along the lines of constant $\Theta_{\rm lab}$ together with the increasing dominance of cascading products in the far backward region. In fact cascading products are found at $x_{\rm F} < -1.0$ which is not accessible for target fragmentation. $R_{\rm casc}$ therefore tends to diverge towards this limit. The arrows given in Fig. 21 indicate the $p_{\rm T}$ value at which $x_{\rm F}$ of -0.85 is reached.

The dependence on $p_{\rm T}$ at fixed $\Theta_{\rm lab}$ can be transformed into a dependence on $x_{\rm F}$ at fixed $p_{\rm T}$ by using eye-ball fits through the data points of Fig. 21 for interpolation. The result is shown in Fig. 22.

Within the sizeable error bars of the data points and the interpolation used, a universal curve appears which clearly shows convergence towards $R_{\rm casc} = 1$ at $x_{\rm F} = 0$. In fact the constraint of $R_{\rm casc}$ to 1 at $x_{\rm F} = 0$ is justified by the fact that relatively large values of $p_{\rm lab}$ are requested to approach $x_{\rm F} = 0$, see Fig. 20. As the ratio $R_{\rm casc}$ gives directly the excess of particle yield due to cascading with respect to target fragmentation, it may be argued that the cascading contribution is only on a few percent level at $x_{\rm F} = -0.1$, that is, at the NA49 acceptance limit. The fact that this acceptance limit applies to $p_{\rm T} = 0.4\,{\rm GeV}/c$ or $p_{\rm lab} = 0.6\,{\rm GeV}/c$ further reduces the possible contribution to the NA49 data. The extrapolation into the unmeasured region used in the preceding sections, which is oriented towards target fragmentation alone, is therefore justified. It should be mentioned here that in the region $x_{\rm F} < -0.1$ and $p_{\rm T} < 0.2$, effects concerning the π^+/π^- ratio must be present due to the final-state Coulomb interaction with

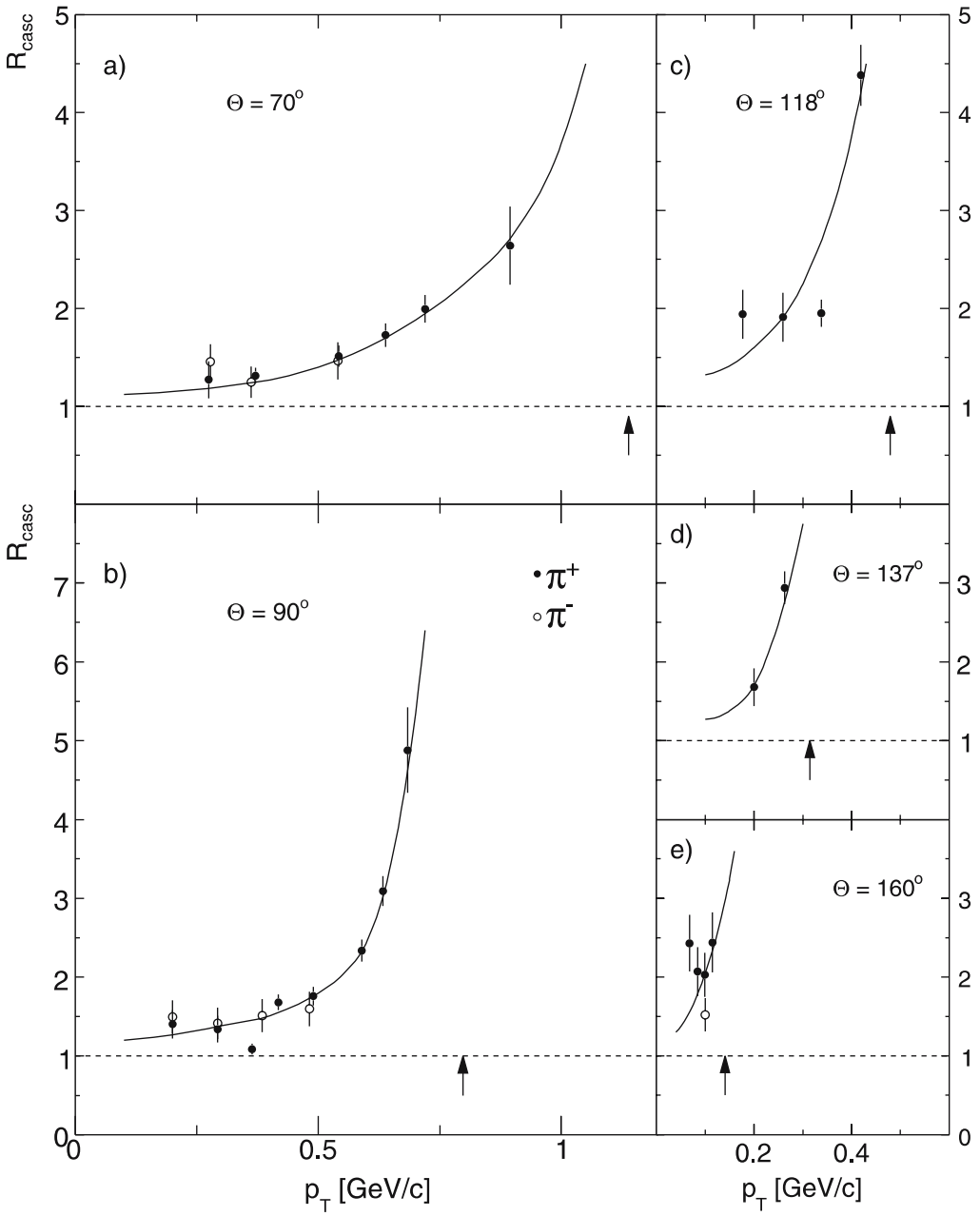

Fig. 21. $R_{\rm casc}$ for different fixed lab angles $\Theta_{\rm lab}$ measured by [24]. The *arrows* indicate the $p_{\rm T}$ value at which $x_{\rm F}$ of -0.85 is reached

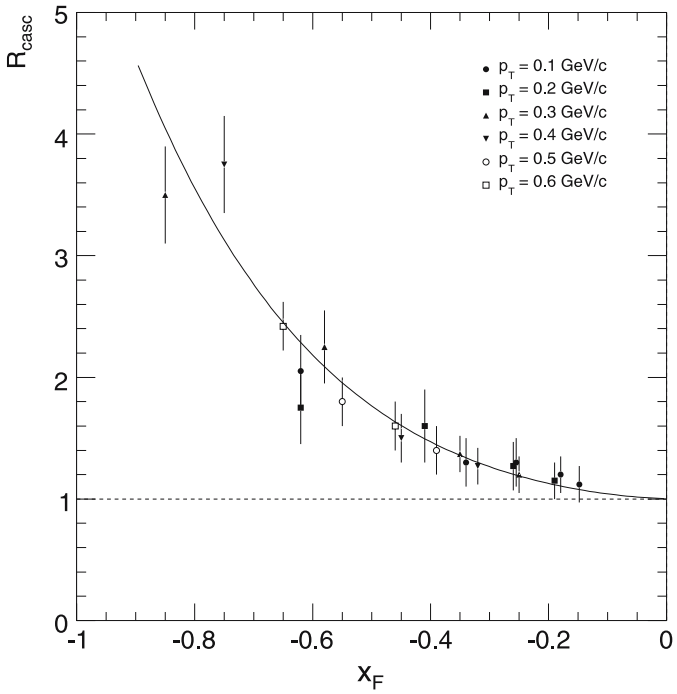

Fig. 22. $R_{\rm casc}$ obtained from [24] as a function of $x_{\rm F}$

the spectator protons in the nucleus [25–28]. These effects are however expected to be small for the light carbon nucleus.

In Sect. 4 above a quantitative prediction from target and projectile fragmentation alone has been given extending into the far backward region $x_{\rm F} < -0.1$. This prediction must now be completed taking account of the cascading contribution as quantified in Fig. 22 above. This correction has been performed for the pion yield ratio $R_{\rm pred}$ shown in Fig. 12 for the charge averaged pion yields where it developed a plateau in this region. The complete prediction is presented in Fig. 23.

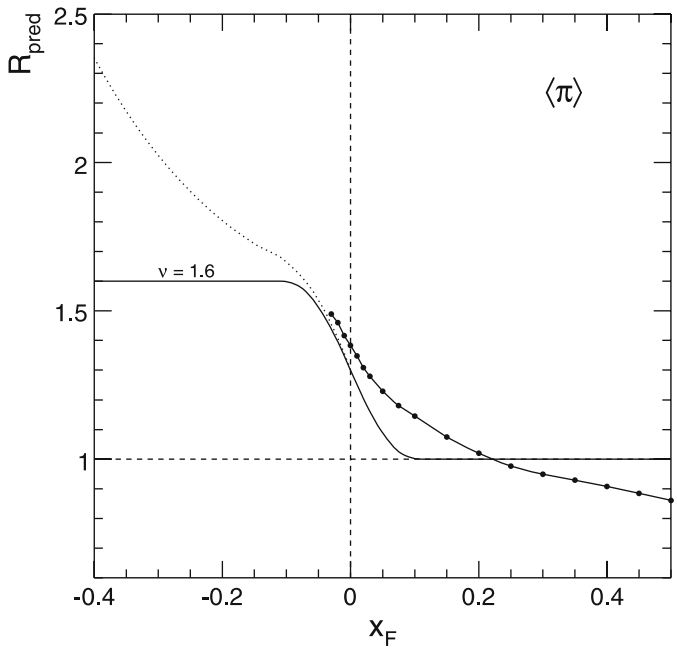

Fig. 23. $R_{\rm pred}$ as a function of $x_{\rm F}$, giving the data points together with the target contribution at $\langle\nu\rangle = 1.6$ (*full line*) and adding the intranuclear cascading part (*broken line*)

In this plot, all three principle contributions to the total pion yield, i. e. projectile and target fragmentation, and nuclear cascading, are clearly discernible and quantified. The resulting overall ratio to the elementary collision exhibits a smooth increase from the far forward to the far backward region in $x_{\rm F}$. This is in agreement with the pseudo-rapidity η ratio

$$R(\eta) = \frac{({\rm d}n/{\rm d}\eta)^{\rm pA}(\eta)}{({\rm d}n/{\rm d}\eta)^{\rm pN}(\eta)} \qquad (16)$$

observed in emulsion work [29] at 200 and 800 GeV/c beam momentum. Also here a quasi-linear increase of $R(\eta)$ is observed, from values below 1 at forward rapidity to values in excess of 2 in the far backward hemisphere.

7 Contribution from multiple collisions

As discussed in Sect. 5 and due to the important tail of the nuclear density profile of the carbon nucleus, a large fraction of all events correspond to a single proton–nucleon collision in a minimum-bias p+C experiment. This probability $P(1)$ is located between 56 and 60% corresponding to a reasonable choice of nuclear density distributions (see Sect. 5 and Fig. 16). Although these single collisions can be accompanied by some amount of nuclear cascading due to the single recoil nucleon, this component will not influence the measurements in the NA49 acceptance region (see Sect. 6). Given $P(1)$, it is therefore possible to extract from the data the content of multiple collisions with $\nu > 1$ which will then rather correspond to a mean value $\langle\nu\rangle \sim 2.5$ (Fig. 19).

In a first example the extraction is applied to the charge averaged density ratio $R(x_{\rm F})$ as defined in (2) above. In this case the multiple collision component is defined as

$$R_{\rm mult}(x_{\rm F}) = \frac{({\rm d}n/{\rm d}x_{\rm F})^{\rm pC}_{\rm mult}(x_{\rm F})}{({\rm d}n/{\rm d}x_{\rm F})^{\rm pp}(x_{\rm F})} = \frac{R(x_{\rm F}) - P(1)}{1 - P(1)} \qquad (17)$$

and is presented in Fig. 24 as a function of $x_{\rm F}$.

In comparison to the minimum-bias measurement, $R_{\rm mult}(x_{\rm F})$ steepens up and reaches the values 2.5 at $x_{\rm F} = -0.1$ and 0.65 at $x_{\rm F} = 0.5$. It is interesting to regard the limit $x_{\rm F} \to 1$. Even if the suppression of pion density in the far forward region of p+A collisions did not as yet find a satisfying explanation, most of the possibilities will finally empty the large $x_{\rm F}$ region of pions from multiple collisions. This is true for projectile energy loss where the scale of $x_{\rm F}$ will change, as well as for baryon transfer processes ("stopping"), should baryonic resonance decay be the source of forward pions. In

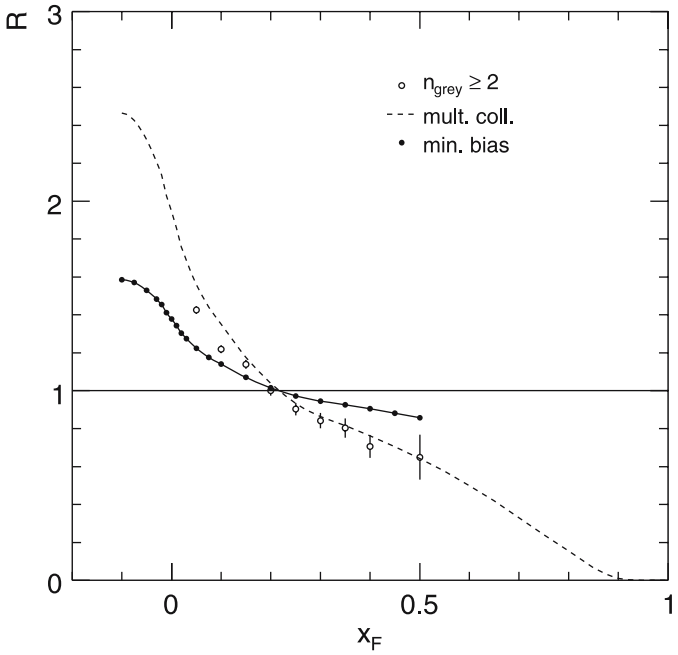

Fig. 24. Prediction for $R_{\rm mult}(x_{\rm F})$ compared with measurement for minimum-bias and $n_{\rm grey} \geq 2$

these cases $R_{\rm mult}(x_{\rm F})$ will approach zero and $R(x_{\rm F} \to 1)$ will reach $P(1)$. This can finally provide a direct measurement of this probability. Figure 24 contains in this sense a tentative extrapolation of $R_{\rm mult}(x_{\rm F})$ towards zero to illustrate the situation which will be further constrained by the upcoming publication of proton data in p+C interactions and of comparable data from p+Pb collisions.

A sharp test of this extraction procedure is given by the data sample with centrality constraint also available from NA49 [3]. Here the additional measurement of slow ("grey") protons in the lab momentum range below 1.2 GeV/c provides an event sample where single collisions should be rather effectively suppressed. The data points shown in Fig. 24 come from events with at least two grey protons detected. As the pion densities for this relatively small subsample have been determined in [3], the ratio

$$R_{\rm grey}(x_{\rm F}) = \frac{({\rm d}n/{\rm d}x_{\rm F})^{\rm pC}_{\rm grey}(x_{\rm F})}{({\rm d}n/{\rm d}x_{\rm F})^{\rm pp}(x_{\rm F})} \tag{18}$$

can be obtained. Evidently this measurement approaches the predicted behaviour for multiple collisions rather closely and proves both the effectiveness of this way of experimental centrality control [22, 30] and the reliability of the prediction of $P(1)$ from nuclear parameters.

As a second example for the extraction of improved information on multiple collisions the evolution of the mean transverse momentum with multiple collisions will be discussed. The situation is shown in Fig. 25 where $\langle p_{\rm T} \rangle$ is shown for p+p collisions [2], minimum-bias p+C interactions [3] and for the event sample with at least two grey protons discussed above.

Evidently the increase of $\langle p_{\rm T} \rangle$ from elementary to minimum-bias nuclear reactions is accentuated imposing centrality control. The multiple collision part can also be extracted from the single collision probability $P(1)$ via the formula

$$\langle p_{\rm T} \rangle^{\rm mult} = \frac{\langle p_{\rm T} \rangle^{\rm pC} - P(1) r \langle p_{\rm T} \rangle^{\rm pp}}{1 - P(1) r}, \tag{19}$$

where $r = ({\rm d}n/{\rm d}x_{\rm F})^{\rm pp}/({\rm d}n/{\rm d}x_{\rm F})^{\rm pC} = 1/R(x_{\rm F})$.

The result is shown as the upper line in Fig. 25. Again both the measurement with grey proton constraint and the prediction from nuclear parameters are coming close.

A third example of this kind will be discussed in connection with the increase of pion yield with transverse momentum in Sect. 8 below.

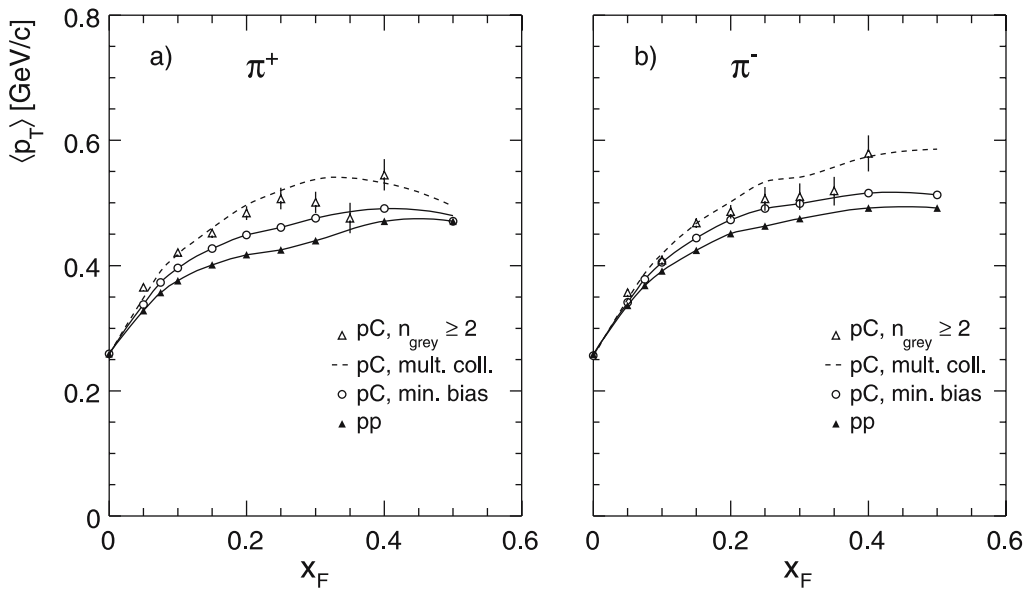

Fig. 25. Prediction for $\langle p_{\rm T} \rangle$ in multiple collisions compared with measurement in p+p, p+C minimum-bias, and p+C with selected number of grey protons $n_{\rm grey} \geq 2$

8 p_T dependence: Cross section ratio with respect to elementary collisions as a function of p_T

Extending the discussion from p_T integrated information to p_T dependent quantities opens up a new and more complex subsurface of the multidimensional phase space as it is projected into the double inclusive cross section

$$f(x_F, p_T) = E(x_F, p_T)\frac{d^3\sigma}{dp^3}(x_F, p_T). \quad (20)$$

Indeed already the superficial inspection of this quantity in its x_F and p_T dependence for p+p [2] and p+C [3] interactions reveals significant local structure which has a different x_F and p_T dependence for the two reactions. In the following sections only a restricted number of phenomena can be touched upon, with the aim at bringing out as clearly as possible some important features which are specific to p+A collisions and therefore also relevant for the subsequent work on p+Pb and Pb+Pb interactions. The discussion will be conducted again in relation to the precise elementary reference given by the NA49 data on p+p collisions [2].

8.1 Definition of the cross section ratio

The presence of the carbon nucleus and of the corresponding two-component hadronization mechanism discussed in the preceding sections implies that the straight-forward cross section ratio

$$R(x_F, p_T) = \frac{f^{pC}(x_F, p_T)}{f^{pp}(x_F, p_T)} \quad (21)$$

is probably not the best choice for describing the full x_F scale. There are in fact two important and well quantified overall phenomena which should and can be taken out in the comparison:

- The target pile-up corresponding to the 1.6 participant nucleons which introduces an x_F-dependent overall upward shift of R in the region $x_F < 0.1$ as elaborated in Sect. 4.
- The isoscalar nature of the carbon nucleus which averages both pion charges in the target contribution, as opposed to the projectile fragmentation.

In order to characterize the projectile-connected p_T dependencies in an optimal way, a definition of the cross section ratio that takes direct reference to the two-component superposition, has been chosen:

$$R_{p_T}(x_F, p_T) = \frac{f^{pC}(x_F, p_T)}{f_{\text{two-comp}}(x_F, p_T)}, \quad (22)$$

where $f_{\text{two-comp}}(x_F, p_T)$ is defined as

$$f_{\text{two-comp}}(x_F, p_T) = t(x_F)\left(\frac{1}{2}f^{pp}_{\pi^+}(x_F, p_T) + \frac{1}{2}f^{pp}_{\pi^-}(x_F, p_T)\right) + p(x_F)f^{pp}(x_F, p_T), \quad (23)$$

with $f^{pp}(x_F, p_T)$ denoting the double differential pion cross section in p+p interactions and R_{p_T}, f^{pC}, $f_{\text{two-comp}}$ and f^{pp} to be regarded separately for π^+ and π^- mesons. The functions $t(x_F)$ and $p(x_F)$ describe the relative contribution of the target and projectile fragmentation to the overall pion yield in the two-component picture, Sects. 3 and 4 above, as recalled in Fig. 26. This corresponds to (10) with $t(x_F)(0.5f^{pp}_{\pi^+} + 0.5f^{pp}_{\pi^-}) \to \langle\nu\rangle(dn/dx_F)^{pp}_{\text{target}}$ and $p(x_F)f^{pp}(x_F, p_T) \to (dn/dx_F)^{pp}_{\text{proj}}$.

Evidently, $t(x_F)$ ensures that the target contribution amounts to $\langle\nu\rangle$ times the average pion yield at $x_F < -0.1$ and vanishes at $x_F = 0.1$. On the other hand $p(x_F)$ determines the total yield at $x_F > 0.1$ and vanishes towards $x_F = -0.1$. The ratio R_{p_T} therefore contains the salient features of the superposition of elementary components in the p+C interaction and addresses specifically the modifications due to the projectile fragmentation. This is shown in Fig. 27 for three values of x_F and for both π^+ and π^-.

Here the full lines represent R_{p_T} using the x_F/p_T interpolation developed for the p+p [2] and p+C [3] interactions. As expected, complex p_T and x_F dependencies emerge. The p_T range around the mean values $\langle p_T\rangle$, indicated by arrows in the plots, governs the p_T integrated yields. It reproduces the features of this quantity in relation to the elementary collisions as elaborated above, namely an increase below $x_F = 0.2$ followed by a zero-crossing and a decrease in the far forward region.

The relative p_T dependence of R_{p_T} in the vicinity of $\langle p_T\rangle$ shows a rather complicated evolution. As the fine structure of $f^{pp}(x_F, p_T)$ and $f^{pC}(x_F, p_T)$ has been con-

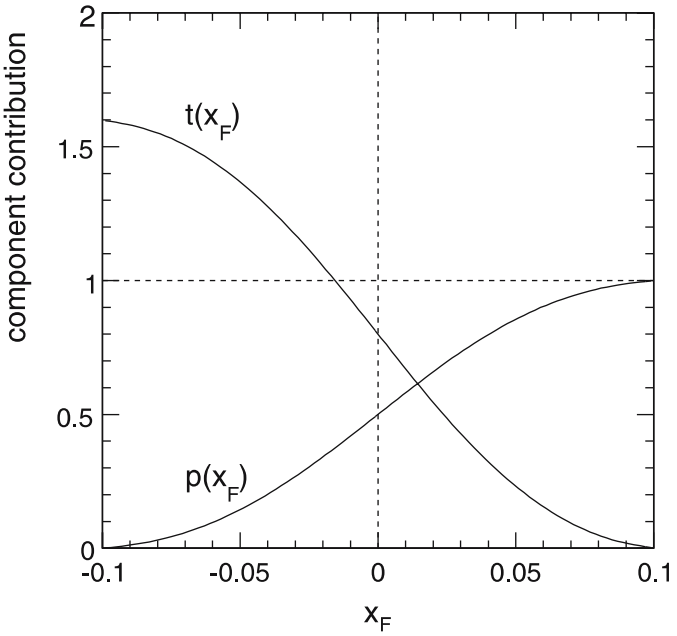

Fig. 26. Target $t(x_F)$and projectile $p(x_F)$ contributions to the pion yield in the two-component picture, with $t(x_F) = 1.6p(-x_F)$

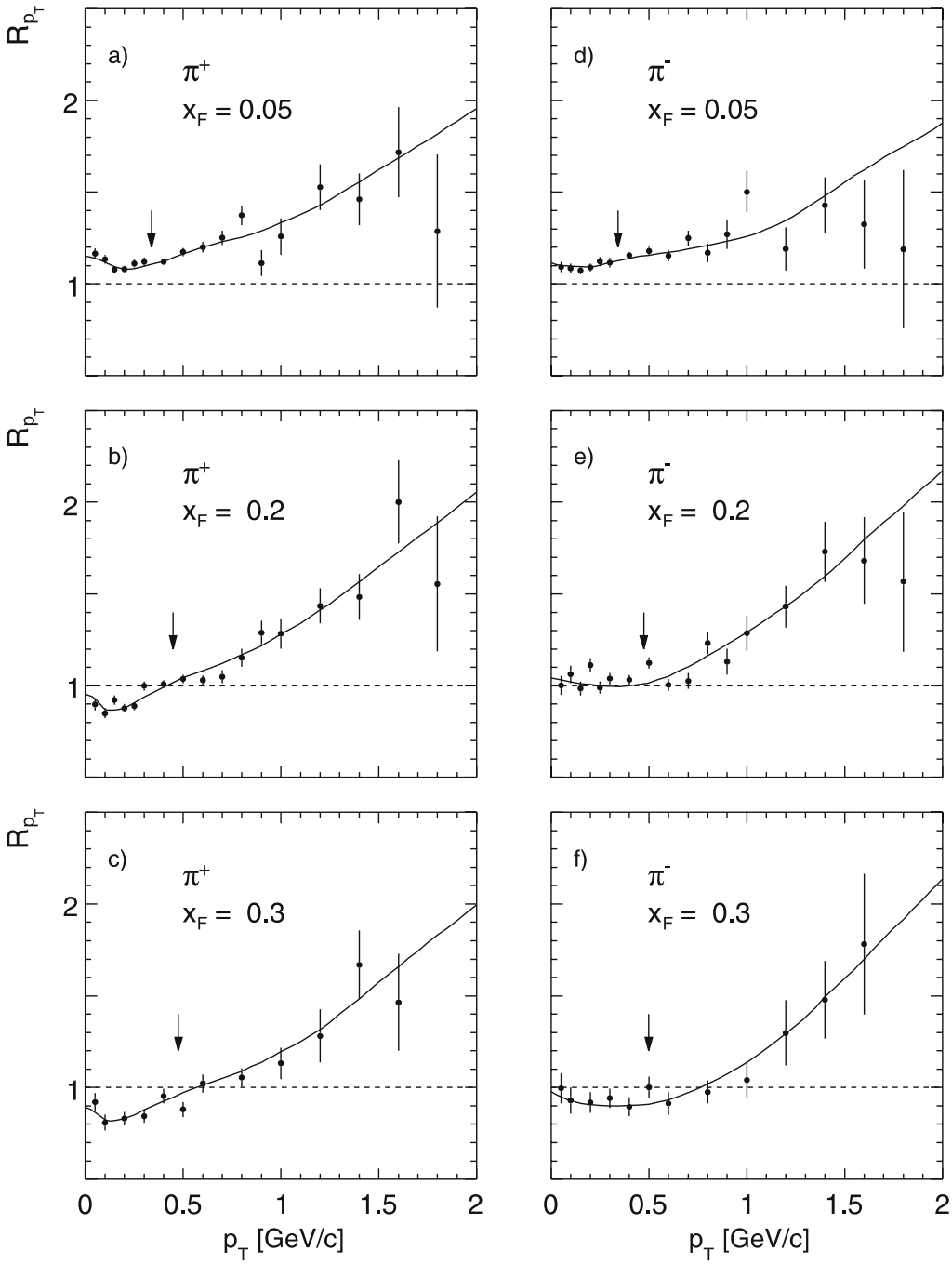

Fig. 27. Ratio R_{p_T} as a function of p_T at three x_F values for **a**–**c** π^+, and **d**–**f** π^-. The *arrows* indicate $\langle p_T \rangle$ for given x_F

nected to resonance production and decay [2], this means that the principle source of pion production changes its composition in p+A interactions both as a function of x_F and of p_T, and in a different way for the two pion charges. Here the attention should be drawn specifically to the behaviour at low p_T governed by the cascading decay of low mass resonances.

A second region of interest is the evolution towards high values of p_T. A significant increase of R_{p_T} with respect to its value at $\langle p_T \rangle$ is evident over the full x_F scale as shown in Fig. 28 which provides an overview of $R_{p_T}(x_F, p_T)$ covering now the full range of the measurements.

8.2 Definition of the p_T enhancement

In order to assess the increase of the pion yields as a function of transverse momentum, the measured enhancement factor $E^m_{p_T}$ is defined as

$$E^m_{p_T}(p_T) = \frac{R_{p_T}(p_T)}{R_{p_T}(\langle p_T \rangle)}. \quad (24)$$

This definition relates the behaviour at any p_T to the mean transverse momentum (see Sect. 7). By referring to an integrated quantity which is representative for the p_T

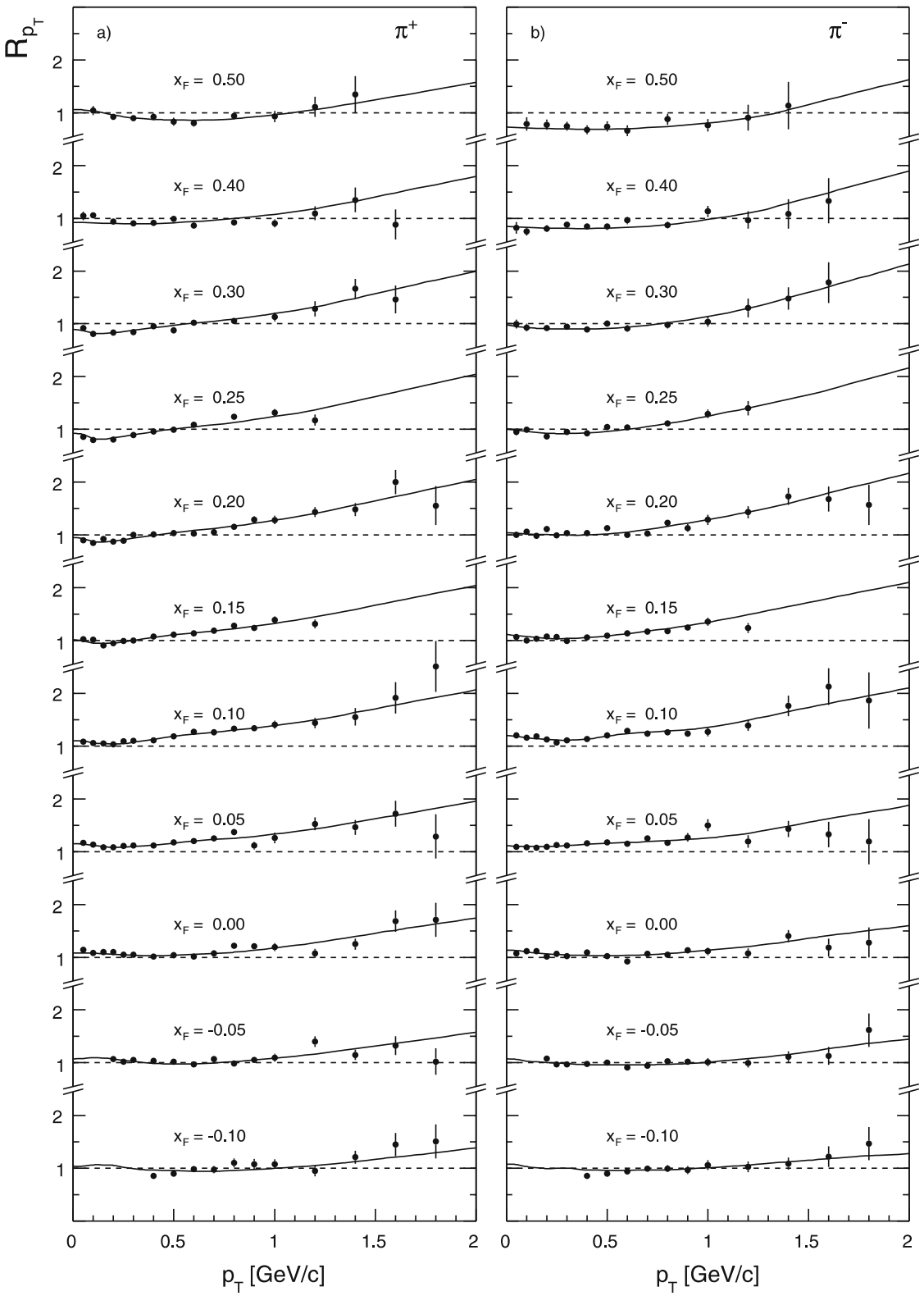

Fig. 28. Ratio $R_{p_{\mathrm{T}}}$ as a function of p_{T} at fixed x_{F} for **a** π^+ and **b** π^-

integrated observables discussed in Sect. 2, the detailed structures which are present at low p_{T} are averaged out in the reference. The x_{F} dependence of $E^m_{p_{\mathrm{T}}}$ is shown in Fig. 29 for four values of p_{T} extending up to the experimental limit at 1.8 GeV/c, and using the interpolation shown in Fig. 28 for the determination of $E^m_{p_{\mathrm{T}}}$.

The shaded regions in Fig. 29 correspond to the estimation of the statistical error margins connected with the in-

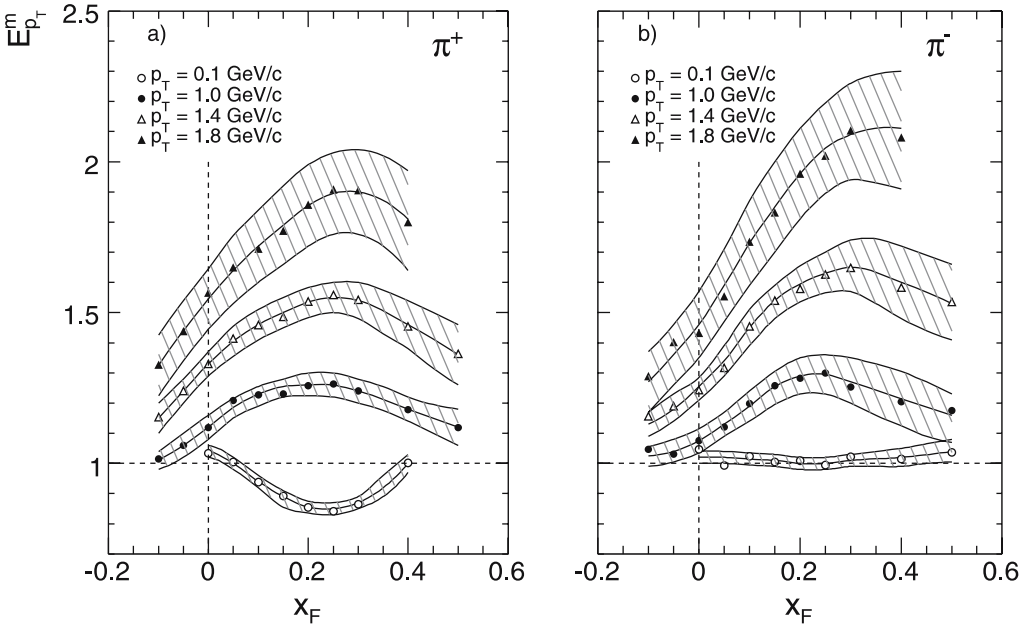

Fig. 29. The p_{T} enhancement as a function of x_{F} at several fixed p_{T} values. The *shaded regions* mark the error margins connected to the interpolation scheme [2, 3]

terpolation procedure. The enhancement factor increases, from values close to unity but significantly different for π^+ and π^- at low p_{T}, up to about 2 at $p_{\mathrm{T}} = 1.8\,\mathrm{GeV}/c$. The increase shows a strong x_{F} dependence, rising from the acceptance limit at $x_{\mathrm{F}} = -0.1$ through $x_{\mathrm{F}} = 0$ towards the forward direction. At $x_{\mathrm{F}} > 0.2, 0.3$, a decrease of $E^m_{p_{\mathrm{T}}}$ is visible.

These effects will be discussed in more detail for the high p_{T} limit in the following section.

9 High p_{T} phenomena

In connection with the discussion of p_{T} dependencies, in particular for proton–nucleus interactions, the term "high p_{T}" needs some specification.

In a first instance, it seems to be a generally accepted notion that hadron production in the region of $p_{\mathrm{T}} \sim 2\,\mathrm{GeV}/c$ is already governed by hard parton-parton scattering. This expectation was first developed in connection with ISR data [31, 32] and is still heavily used in the interpretation of very recent RHIC results [33, 34]. The notion "high" therefore tends to be synonymous with the applicability of perturbative QCD, although there is no indication of any serious experimental proof for this assumption.

In a second instance, the early discovery of an "anomalous" p_{T} enhancement in proton–nucleus collisions, the so-called Cronin effect [35], in a corresponding region of transverse momentum, seems to point again into the same direction. In fact the only theoretical attempts at an understanding of the Cronin effect are based on multiple partonic scattering [36–40]. And again the present experimental information does not permit in the least to affirm this conjecture.

In the context of this paper the notion "high" p_{T} describes the upper limit of p_{T} available to NA49 in the p+C interaction. The authors consider any relation of this notion to perturbative effects as an unfounded speculation.

9.1 Anomalous nuclear enhancement

The anomalous nuclear enhancement was first quantified via the A-dependence of hadronic cross sections, parametrized as

$$\sigma^{\mathrm{pA}} \sim A^{\alpha(p_{\mathrm{T}})}. \tag{25}$$

The dependence of the exponent α on transverse momentum [35] is recalled in Fig. 30 for π^+ and π^-.

The exponent $\alpha(p_{\mathrm{T}})$ rises steeply from values between 0.8 and 0.9 at low p_{T} to a maximum of about 1.15 at $p_{\mathrm{T}} \sim 4\,\mathrm{GeV}/c$. Above this p_{T} the exponent decreases again. The scarce measurements and the sizeable error bars at $200\,\mathrm{GeV}/c$ beam momentum, i. e. in the immediate vicinity of the NA49 data set, do not exclude a sizeable s-dependence. It is also visible in Fig. 30 that α is slightly larger for π^- than for π^+. As regards the upper p_{T} limit of the NA49 data at $1.8\,\mathrm{GeV}/c$, Fig. 30, the corresponding $\alpha(p_{\mathrm{T}})$ is about half-way up from the low-p_{T} value to the saturation limit. It happens to be very close to unity, a value that was believed to be characteristic of hard parton scattering [35]. The detailed study of the nuclear enhancement in this p_{T} region gives therefore already valuable information concerning the understanding of the Cronin effect.

The cross sections measured by [35] for Be, Ti and W nuclei may be interpolated to carbon and compared directly to the NA49 data. This comparison is shown in Fig. 31 for $\langle\pi\rangle$.

Unfortunately there is only one overlapping data point at $200\,\mathrm{GeV}/c$ beam momentum in the p_{T} range of NA49, and the consistency of the few data points at $400\,\mathrm{GeV}/c$

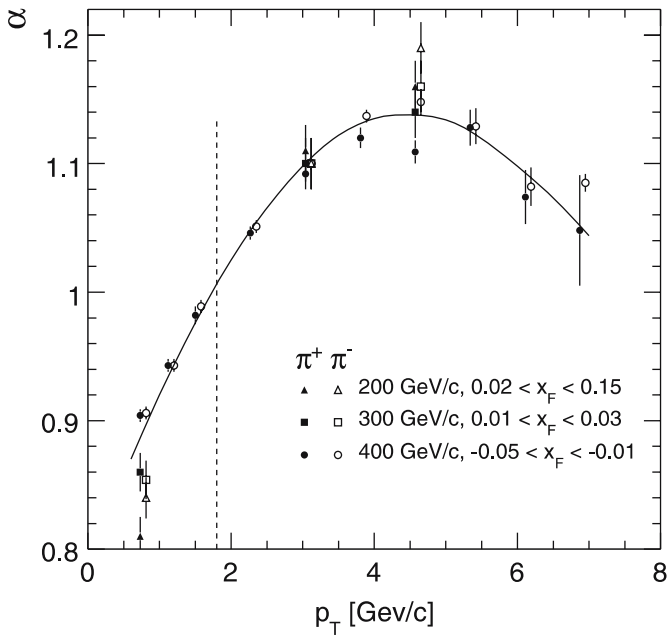

Fig. 30. The exponent α as a function of p_{T}. The *dashed line* corresponds to the p_{T} limit of the NA49 data

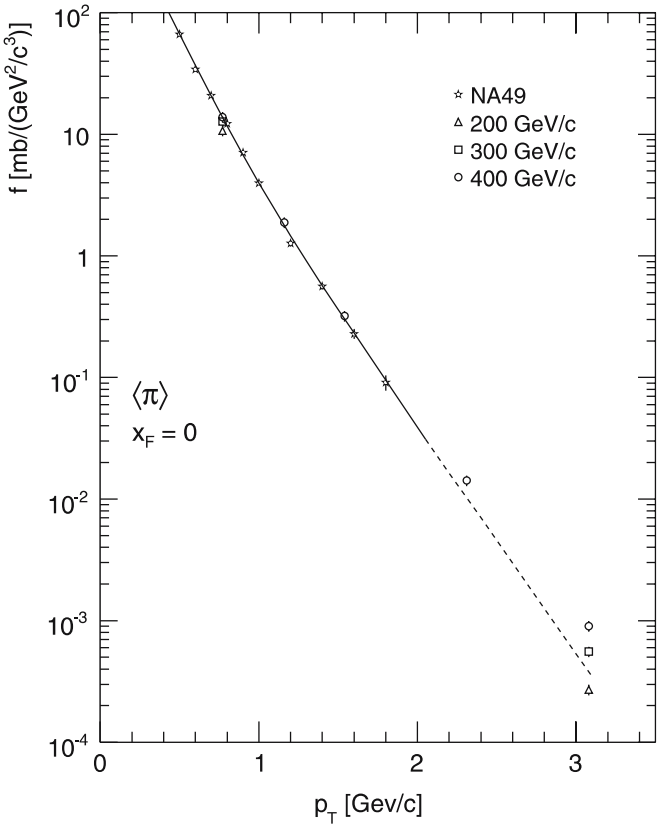

Fig. 31. Comparison of the cross section for $\langle\pi\rangle$ as a function of p_{T} at $x_{\mathrm{F}} = 0$ measured by [35] and interpolated to carbon with p+C results from NA49

is not really expected due to the strong non-scaling behaviour of the s-dependence in their p_{T} range. In this context it must be recalled that the data of [35] have been obtained at a constant lab angle of 77 mrad which leads to an s-dependent spread of the corresponding x_{F} values between -0.05 and $+0.15$, see Fig. 30. In view of the strong x_{F} dependencies of both the target pile-up, Fig. 23, and the nuclear enhancement, Fig. 31, this leads to systematic effects which are non-negligible at the level of precision of the present study. Including however the 20% normalization uncertainties quoted by [35] and the sizeable statistical errors of these measurements, the consistency of the data may still be considered as satisfactory.

9.2 Two basic contributions to the high p_{T} enhancement

Turning back to the NA49 data, it may be claimed that they permit the first systematic study of the x_{F} dependence of the Cronin effect, as the data of [35] only cover a small, s and p_{T} dependent x_{F} range. The new data at forward rapidity available from d+Au collisions at RHIC energy suffer from missing acceptance at low p_{T}. They will be commented on in a subsequent section of this paper.

Inspection of Fig. 29 shows that the central region of particle production occupies by no means a special place, as the enhancement rises smoothly through $x_{\mathrm{F}} = 0$ and has its maximum in the region around $x_{\mathrm{F}} = 0.3$ which is far forward with respect to the longitudinal evolution of pion yields. This behaviour indicates two important facts:

– $E^m_{p_{\mathrm{T}}}$ converges towards unity in the backward region, $x_{\mathrm{F}} < -0.1$.

– $E^m_{p_{\mathrm{T}}}$ tends as well towards unity in the far forward region, $x_{\mathrm{F}} > 0.4$.

In a two-component superposition scheme, the first phenomenon is indeed expected in the negative x_{F} limit where the projectile component vanishes with respect to the target contribution. In this picture there is no reason to believe that the fragmentation of the participant target nucleons shows anomalous behaviour at high p_{T}. In other words the target enhancement factor $E^{\mathrm{target}}_{p_{\mathrm{T}}}$ should be equal to one over the full x_{F} range. The superposition should be characterized by target and projectile components with a specific x_{F} dependence, as presented in Fig. 32 b.

The second phenomenon is of different origin. It is connected to the large probability of single collisions, $P(1)$, in minimum-bias proton–nucleus interactions, as discussed in Sects. 3 and 7 above. It has been shown there that the contribution from single collisions grows as $x_{\mathrm{F}} = 1$ is approached since the pion yield from multiple collisions is progressively suppressed at large x_{F}. As $E^m_{p_{\mathrm{T}}}$ is unity for single collisions, the enhancement should tend towards one for large x_{F}. The influence of $P(1)$ on the variation of the measured enhancement with x_{F} can be described by a multiplicative weight function $\epsilon(x_{\mathrm{F}})$ as shown in Fig. 32 c. This function approaches the value of $1.6 \sim 1/P(1)$ for $x_{\mathrm{F}} \to 1$ and reduces to ~ 0.9 in the backward region due to the yield increase from the projectile fragmentation.

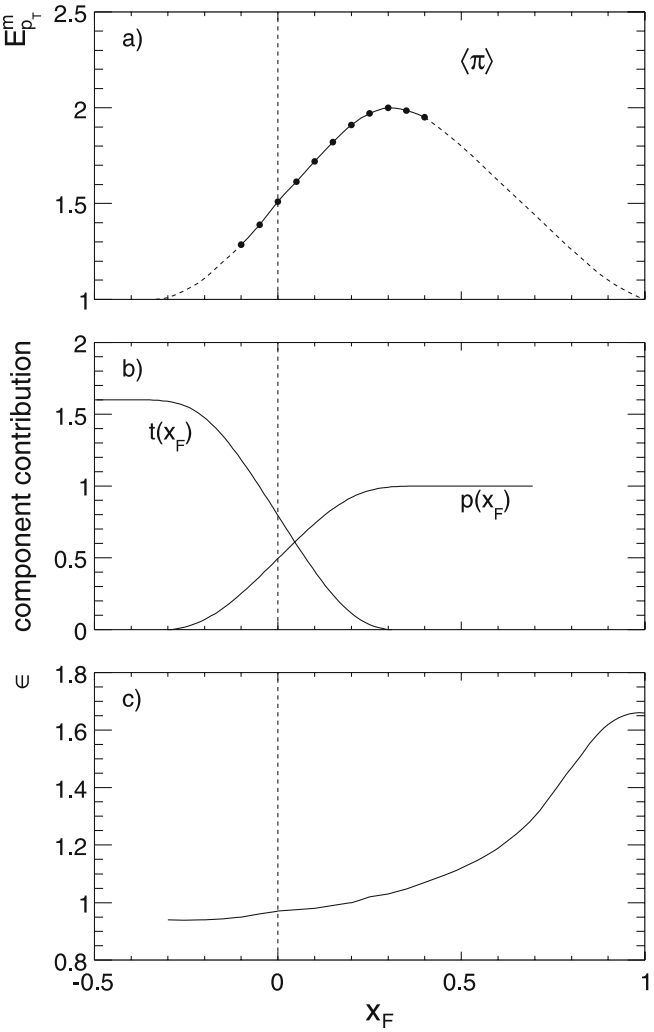

Fig. 32. a The enhancement factor $E^m_{p_T}$ as a function of x_F for $\langle\pi\rangle$ at $p_T = 1.8$ GeV/c, **b** target and projectile contributions as a function of x_F at $p_T = 1.8$ GeV/c, and **c** weight function ϵ multiplying the relative contribution from single collisions as a function of x_F

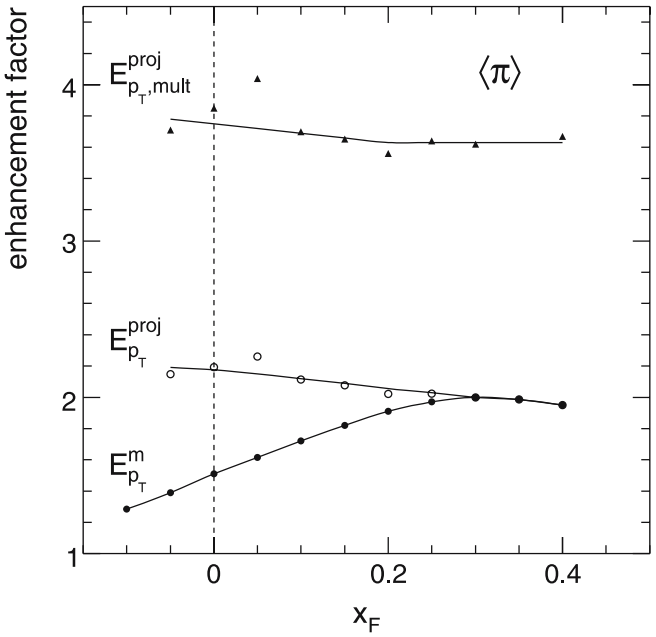

Fig. 33. The enhancement factors $E^m_{p_T}$, $E^{proj}_{p_T}$, $E^{proj}_{p_T,\nu\geq 2}$ as a function of x_F at $p_T = 1.8$ GeV/c

9.3 Extraction of the projectile component

Concerning the target-projectile superposition, it can be stated that the range of the corresponding target-projectile feed-over is larger than at low transverse momentum (Sect. 4) and reaches $x_F \sim \pm 0.3$. This indicates an important p_T dependence, Fig. 29 and Sect. 10. This is quantified by writing down the composition of the measured enhancement $E^m_{p_T}$ from the target ($E^{target}_{p_T} = 1$) and the projectile ($E^{proj}_{p_T}$) components:

$$E^m_{p_T} = \frac{t(x_F)E^{target}_{p_T} + r_{proj}E^{proj}_{p_T}}{t(x_F) + r_{proj}}, \qquad (26)$$

where $r_{proj} = (dn/dx_F)^{pC}_{proj}(\langle p_T\rangle)/(dn/dx_F)^{pp}(\langle p_T\rangle)$. Here $t(x_F)$ and $p(x_F)$ specify the shape of the relative target and projectile contributions as a function of x_F at $p_T = 1.8$ GeV/c. The components $t(x_F)$ and $p(x_F)$ reach further out in x_F, Fig. 32 b, than at low p_T, Fig. 9. They are constrained by the boundary conditions $p(-0.3) = t(0.3) = 0$ and $p(x_F > 0.3) = 1$, $t(x_F < -0.3) = \langle\nu\rangle$, and the symmetry conditions $p(0) = 0.5$ and $t(0) = \langle\nu\rangle/2$ as indicated in Fig. 32. Evidently these functions are more similar to the proton than to the low-p_T pion feed-over shown in Fig. 11. The enhancement factor for the projectile component can be extracted from (26) as

$$E^{proj}_{p_T} = \frac{1}{r_{proj}}\left(E^m_{p_T}(t(x_F) + r_{proj}) - t(x_F)\right). \qquad (27)$$

The x_F dependence of $E^{proj}_{p_T}$ is presented in Fig. 33.

As an important consequence of this decomposition it appears that the measured nuclear enhancement at $x_F = 0$ is not fully representative of the phenomenon. It is very substantially increased if proper account is taken of the "inert" target contribution in p+A reactions. This is very important for the understanding of the nuclear enhancement in the symmetric A+A interactions where the target and projectile contribution are equally contributing. From this consideration alone it must be expected that the measured nuclear enhancement in A+A collisions must be larger than in p+A collisions. If however properly extracting the projectile component the enhancement should tend to be equal in both types of reaction at equal $\langle\nu\rangle$ per projectile (p+A) or participant (A+A), unless new physics phenomena should be present in A+A interactions.

9.4 Enhancement due to multiple collisions

The influence of single collisions on the measured nuclear enhancement is particularly important in the p+C case

discussed here, as the probability $P(1)$ is about 0.6 and the corresponding enhancement should be unity for this contribution. Taking account of the weight function $\epsilon(x_{\rm F})$ introduced above, the enhancement due to multiple collisions can be extracted as

$$E^{\rm proj}_{p_{\rm T},{\rm mult}}(x_{\rm F}) = \frac{E^{\rm proj}_{p_{\rm T}}(x_{\rm F}) - P(1)\epsilon(x_{\rm F})}{1 - P(1)\epsilon(x_{\rm F})} \qquad (28)$$

The application of (28) results in a further, very considerable increase of the nuclear enhancement over the full $x_{\rm F}$ range as evident from Fig. 33. The final result for $E^{\rm proj}_{p_{\rm T},{\rm mult}}$ is very different indeed from the measured quantity $E^{m}_{p_{\rm T}}$. In this context the application of straight-forward parametrizations of the A-dependence, as they are applied in the description of the nuclear enhancement, Sect. 9.1 above, is to be regarded with great caution. This because the probability $P(1)$ depends strongly on A, see Fig. 17. By relating the effect in p+Be to the one in p+W for instance, one compares cases where $P(1)$ differs by a more than a factor of 3. This means that the exponent $\alpha(p_{\rm T})$ will decrease appreciably once the trivial effect of single collisions is taken out.

As far as A+A collisions are concerned, the correct way of comparison would be to relate minimum-bias p+A to minimum-bias A+A collisions where the distributions $P(\nu)$ are equal [16], with ν being defined as a number of collisions per participant nucleon. For centrality selected collisions, this condition is more difficult to fulfill as the probability $P(1)$ stays always greater than zero for A+A interactions even for impact parameter zero, whereas it vanishes for central p+A interactions [16].

9.5 A look at rapidity dependence

The interpretation of the nuclear enhancement as a $p_{\rm T}$ dependent phenomenon necessitates the use of kinematic variables that are orthogonal in the transverse and longitudinal components, as is the case for the $x_{\rm F}/p_{\rm T}$ combination used here. By describing the same phenomenon in the variables rapidity y and $p_{\rm T}$, a completely different picture will emerge as the use of y combines both the transverse and the longitudinal evolution of the particle densities, except, of course, at $y = 0$. This is exemplified in Fig. 34 where the y dependence of the enhancement factor

$$E_y(y, p_{\rm T}) = \frac{R_y(y, p_{\rm T})}{R_y(y, \langle\, p_{\rm T}\rangle)} \qquad (29)$$

with $R_y(y, p_{\rm T}) = ({\rm d}n/{\rm d}x_{\rm F})^{\rm pC}(y, p_{\rm T})/({\rm d}n/{\rm d}x_{\rm F})^{\rm pp}(y, p_{\rm T})$, is presented at the same four values of transverse momentum as shown in Fig. 29.

The strong increase of the nuclear enhancement with $x_{\rm F}$ is replaced by a flat y-dependence up to $y \sim 1$, followed by a strong decrease for $y > 1.5$. From this plot alone one might erroneously conclude that the Cronin effect vanishes in forward direction, whereas is reality one is looking at the longitudinal decrease of particle density in p+A collisions, see Sect. 4 above.

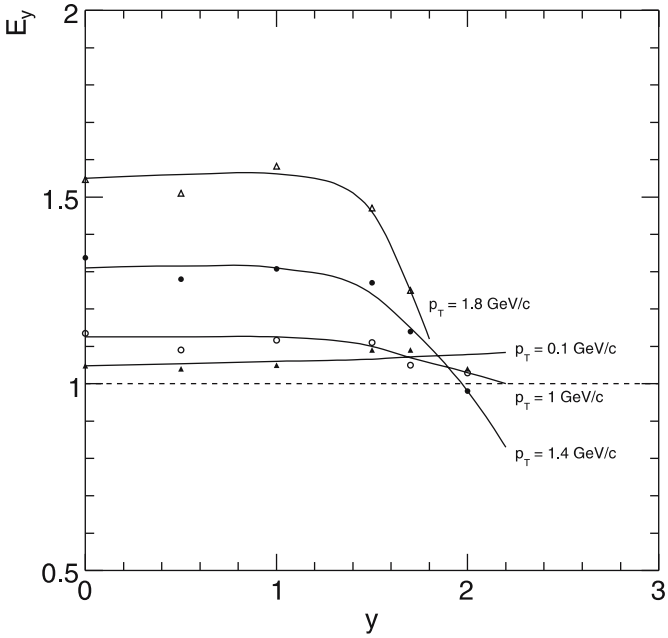

Fig. 34. The $p_{\rm T}$ enhancement as a function of y at several fixed $p_{\rm T}$ values

Experimentally it is often difficult, if not impossible, to fulfill the orthogonality condition mentioned above. This is true for all experiments being limited by a polar angle (or rapidity) cut-off in forward direction, where the low $p_{\rm T}$ region may not be accessible at all above a certain limit of $x_{\rm F}$. This is typical of collider experiments. For the BRAHMS detector at RHIC, for instance, the rapidity limit of 3.2 units corresponds to a $p_{\rm T}$ cut-off at 0.8 GeV/c already at $x_{\rm F} = 0.1$ where the measured nuclear enhancement is still increasing, and at $p_{\rm T} = 2$ GeV/c for $x_{\rm F} = 0.25$ where it reaches its maximum.

10 The trace of resonance decay

The production and decay of resonances constitutes a much neglected but important field of studies concerning soft hadronization. As already pointed out in [2] many details of the inclusive pion distributions directly show the imprint of resonance decay. In the context of the present paper several of the extracted features concerning the two-component nature of the hadronization process will be discussed here in relation to resonance decay. This concerns in particular the following experimental findings:

- The shape and feed-over of the extracted, $p_{\rm T}$ integrated projectile component (Sects. 3 and 4).
- Its dependence on particle mass (Sect. 3.5).
- Its important $p_{\rm T}$ dependence up to the limit of the NA49 data at 1.8 GeV/c (Sect. 9).

As a complete treatment of the manifestations of resonance phenomena exceeds the scope of this paper and has to be left to a coming publication, only some basic mech-

anisms which are of straight-forward kinematic origin will be treated here, using a single resonance as a tool for explanation. The resonance chosen is the $\Delta^{++}(1232)$ whose inclusive $x_{\rm F}$ and $p_{\rm T}$ distributions have been determined in an adequate fashion for the present purpose [41, 42]. Its measured, $p_{\rm T}$ integrated $x_{\rm F}$ distribution is shown in Fig. 35 together with the target and projectile components constructed from it, using the baryonic feed-over shape as discussed in Sect. 3.5. The two-body decay $\Delta^{++} \to {\rm p} + \pi^+$ performed for the projectile component of Fig. 35 yields $p_{\rm T}$ integrated $x_{\rm F}$ distributions of the decay products as shown in Fig. 36.

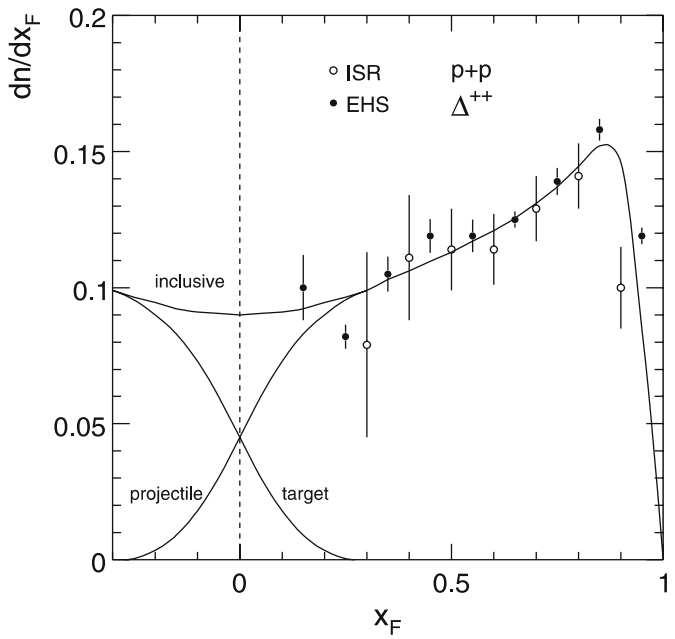

Fig. 35. Two-component picture for Δ^{++}

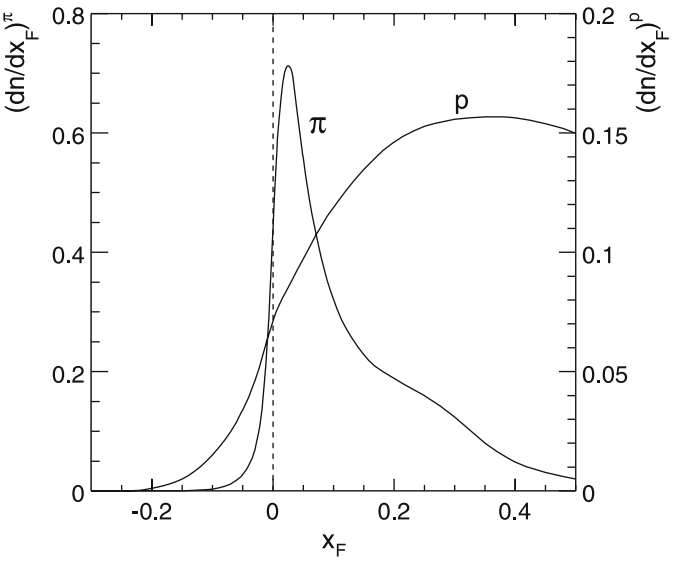

Fig. 36. $p_{\rm T}$ integrated $x_{\rm F}$ distributions of protons and pions produced from Δ^{++} decay

A first observation concerns the overall shape of the π^+ distribution in comparison to the extracted inclusive projectile contributions shown in Figs. 8 and 14. Although there are of course deviations in detail, as to be expected from the single, low-mass resonance studied here, the overall agreement in shape and $x_{\rm F}$-range is very evident. This concerns specifically the limited range of the pion feed-over into the target hemisphere.

A second observation concerns the difference of this feed-over between proton and pion. The mass dependence quantified in Fig. 11b is reproduced insofar as the baryon distribution reaches much further into the opposite hemisphere than for the pion.

This effect is of course a straight-forward consequence of the Lorentz transformation between the resonance rest frame and the overall cms. The energy factor of this transformation reads

$$E = \sqrt{m_{\rm sec}^2 + q^2}, \tag{30}$$

where $m_{\rm sec}$ is the decay particle mass and q is given by

$$q = \frac{1}{2m_{\rm res}} \sqrt{(m_{\rm res}^2 - (m_\pi + m_{\rm p})^2)(m_{\rm res}^2 - (m_\pi - m_{\rm p})^2)}. \tag{31}$$

At the nominal mass of the Δ^{++} this corresponds to $0.229\,{\rm GeV}/c$ which is much smaller than the proton mass. The proton therefore receives, in contrast to the pion, a major fraction of the resonance momentum in the cms of the interaction.

A third observation concerning $p_{\rm T}$ dependence is obtained by studying the Δ^{++} decay for pions in bins of transverse momentum, as shown in Fig. 37.

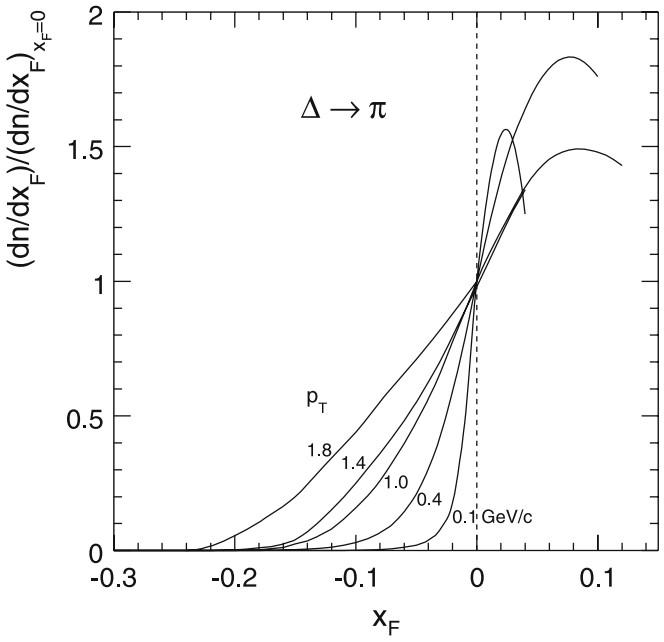

Fig. 37. Pion feed-over from Δ^{++} decay for different values of $p_{\rm T}$

For the same bins used in Fig. 29 above, the distributions are normalized to unity at $x_F = 0$ in order to calibrate the strong p_T dependence of the cross section. Evidently there is a steady increase of the range of feed-over with increasing transverse momentum. The shape dependence of the p_T integrated x_F distributions on the lower integration limit demonstrated in Figs. 2 and 3 finds thereby a natural explanation. At the upper p_T limit of the NA49 data at 1.8 GeV/c, the shape of the pion distribution approaches the one measured for the proton. This effect has been used for the extraction of the projectile component of the p_T enhancement, Fig. 32, by adopting a feed-over distribution which corresponds to the p_T dependence evident in Fig. 37.

This third observation follows again from the resonance decay kinematics. In fact the most efficient way to obtain high transverse momentum for low mass secondaries is to exploit the Breit-Wigner tail of the resonance mass distribution which reaches, in the case of the $\Delta(1232)$, values well above 2 GeV. Correspondingly the decay momentum q (31) increases into the 1 GeV/c region which in turn reduces the mass dependence (30) and increases the range of the feed-over. It is therefore necessary to take proper account of the resonance mass distribution in any quantitative work on hadronization dealing with resonance decay.

Following these observations, resonance decay as a source of "high p_T" production in the sense defined above has to be considered very seriously. Using a sum of 13 measured resonances it has indeed been demonstrated for p+p collisions [43] that the inclusive pion distributions resulting from two body decays saturate the yields up to $p_T = 3$ GeV/c and beyond simultaneously over the full range of x_F. A modification of the resonance spectrum towards higher masses in multiple collisions would therefore be sufficient to also describe the anomalous nuclear enhancement in this p_T range, at SPS energies, without invoking partonic or perturbative effects.

11 Conclusions

This paper attempts a new assessment of the p+A interaction with light nuclei at SPS energy which is based exclusively on experimental data. The study leads to a number of conclusions which cover a wide range of observables. They may be subsummed as follows:

- The reference to a set of experimental results obtained in elementary and nuclear interactions, in particular to the new precision data from the NA49 detector in p+C and p+p collisions, allows for a model independent argumentation.
- This argumentation clearly establishes the composition of the p+A reaction from three basic components: projectile fragmentation, target fragmentation, and intranuclear cascading.
- These contributions have been isolated and quantified one by one.
- Intranuclear cascading governs the far backward hemisphere. Its contribution rapidly decreases towards $x_F = 0$ and corresponds to only a couple of percent relative to the participant fragmentation at $x_F = -0.1$.
- For the remaining target and projectile contributions, a clear two component picture has been established. The two components overlap in a limited zone around $x_F = 0$. The extent of this zone is shown to depend on particle species and transverse momentum. It is limited to $x_F \pm 0.1$ for the p_T integrated pion yield and reaches out to $x_F \pm 0.25$ at p_T of 1.8 GeV/c.
- Target fragmentation reflects the superposition of participant hadronization, revealing the detailed charge dependence introduced by the isospin composition of the nucleus. The total pion yield from this source corresponds to an average of 1.6 participant target nucleons which is close to but significantly below the number expected from measured nuclear parameters.
- The extraction of detailed features of the projectile fragmentation has been the main aim of the study. In relation to elementary collisions a complex pattern of deviations emerges which concerns practically all measured quantities.
- The total pion yield from projectile increases by about 10% as compared to the elementary interaction. This increase is concentrated near $x_F = 0$ with a shape that matches the density distribution of the projectile component.
- Above $x_F \sim 0.2$ the differential yield decreases steadily with respect to elementary collisions as x_F increases, with a specific charge dependence.
- Using the well defined probability for single projectile collisions, the contribution from multiple collisions has been extracted and compared to the centrality controlled p+C data subsample.
- The detailed p_T dependence of the projectile component has been established in comparison to elementary collisions. In the neighbourhood of the mean transverse momentum the comparison is characterized by important, charge dependent local structure. With increasing transverse momentum a general increase of pion yield is established.
- This increase is quantified by an enhancement factor which shows strong x_F dependence and has been corrected for the inert contributions from target fragmentation and from single collisions.
- The relation to the anomalous nuclear enhancement (Cronin effect) is established and it is demonstrated that a new assessment of this phenomenon is mandatory from a purely experimental point of view.
- Finally the importance of resonance production and decay for virtually all studied quantities is evoked.

This study will be continued and deepened by using the data on centrality selected p+Pb and Pb+Pb collisions that are also available from the NA49 experiment.

Acknowledgements. This work was supported by the Polish State Committee for Scientific Research (1 P03B 006 30, 1 P03B 097 29, 1 PO3B 121 29, 1 P03B 127 30), the Hungarian Scientific Research Foundation (T032648, T032293, T043514), the Hungarian National Science Foundation, OTKA,

(F034707), the Polish-German Foundation, the Bulgarian National Science Fund (Ph-09/05), the EU FP6 HRM Marie Curie Intra-European Fellowship Program, and the Particle Physics and Astronomy Research Council (PPARC) of the United Kingdom.

References

1. H.G. Fischer et al., Nucl. Phys. A **715**, 118 (2003)
2. C. Alt et al., Eur. Phys. J. C **45**, 343 (2006)
3. Inclusive production of charged pions in p+C collisions at 158 GeV/c beam momentum (to be published)
4. A. Bialas et al., Nucl. Phys. B **111**, 461 (1976)
5. D. Barton et al., Phys. Rev. D **27**, 2580 (1983)
6. H.G. Fischer et al., Heavy Ion Phys. **17**, 369 (2003)
7. G.J. Bobbink et al., Nucl. Phys. B **204**, 173 (1982)
8. C.M. Bromberg et al., Phys. Rev. D **9**, 1864 (1974)
9. T. Kafka et al., Phys. Rev. Lett. **34**, 687 (1975)
10. V.V. Aivazyan et al., Z. Phys. C **42**, 533 (1989)
11. S. Uhlig et al., Nucl. Phys. B **132**, 15 (1978)
12. K. Guettler et al., Nucl. Phys. B **116**, 77 (1976)
13. R.D. Field, R.P. Feynman, Nucl. Phys. B **136**, 1 (1978)
14. D. Varga, Study of Inclusive and Correlated Particle Production in Elementary Hadronic Interactions, PhD. Thesis (2003) Eötvös Loránd University, Budapest
15. D. Varga et al., Heavy Ion Phys. **17**, 387 (2003)
16. A. Rybicki, H. Niewodniczański, Institute of Nuclear Physics, Internal Report No 1976/PH, http://www.ifj.edu.pl/publ/reports/2006/
17. E.A.J.M. Offermann et al., Phys. Rev. C **44**, 1096 (1991)
18. I. Sick, Phys. Lett. B **116**, 212 (1982)
19. H. Enge, In: Introduction to Nuclear Physics, Addison-Wesley World Student Series, (1972)
20. G. Fricke et al., Atom. Data Nucl. Data **60**, 177 (1995)
21. I. Sick, Nucl. Phys. A **218**, 509 (1974)
22. M.K. Hegab, J. Hüfner, Nucl. Phys. A **384**, 353 (1982)
23. A. Bialas et al., Phys. Lett. B **51**, 179 (1974)
24. N.A. Nikiforov et al., Phys. Rev. C **22**, 700 (1980)
25. J. Burfening et al., Phys. Rev. **75**, 382 (1949)
26. H. Yagoda, Phys. Rev. **85**, 891 (1952)
27. E.M. Friedländer, Phys. Lett. **2**, 38 (1962)
28. N.I. Kostanashvili et al., Sov. J. Nucl. Phys. **13**, 715 (1971)
29. A. Abduzhamilov et al., Phys. Rev. D **39**, 86 (1989)
30. S. Afanasiev et al., Nucl. Instrum. Methods A **430**, 210 (1999)
31. M. Della Negra et al., Nucl. Phys. B **127**, 1 (1977)
32. R.P. Feynman et al., Phys. Rev. D **18**, 3320 (1978)
33. J.J. Gaardhøje et al., Eur. Phys. J. C **43**, 287 (2005)
34. B.Z. Kopeliovich et al., Phys. Rev. C **72**, 054606 (2005)
35. D. Antreasyan et al., Phys. Rev. D **19**, 764 (1979)
36. J. Kühn, Phys. Rev. D **13**, 2948 (1976)
37. A. Krzywicki et al., Phys. Lett. B **85**, 407 (1979)
38. M. Lev, B. Petersson, Z. Phys. C **21**, 155 (1983)
39. A. Accardi, hep-ph/0212148 (2003)
40. B. Kopeliovich et al., Phys. Rev. Lett. **88**, 232303 (2002)
41. A. Breakstone et al., Z. Phys. C **21**, 321 (1984)
42. M. Aguilar-Benitez et al., Z. Phys. C **50**, 405 (1991)
43. H.G. Fischer et al., CERN/SPSC 2005-035